NASA's Black Marble Nighttime Lights Product Suite
Algorithm Theoretical Basis Document (ATBD)

Principal Investigator: Dr. Miguel O. Román

Correspondence e-mail address: Miguel.O.Roman@nasa.gov

Prepared by: Zhuosen Wang, Ranjay Shrestha, and Miguel O. Román

Version 1.1

July 2020

NASA Goddard Space Flight Center

Greenbelt, Maryland

List of Revisions

Version	Revision	Date	Authors
V1.0	(Collection V001 Reprocessing)	April, 2018	Wang, Shrestha, Román
V1.1	(Collection V001 Reprocessing)	July, 2020	Wang, Shrestha, Román

Citation

Román, M.O., Wang, Z., Sun, Q., Kalb, V., Miller, S.D., Molthan, A., Schultz, L., Bell, J., Stokes, E.C., Pandey, B., Seto, K.C., et al. (2018). NASA's Black Marble Nighttime Lights Product Suite. *Remote Sensing of Environment*, 210, 113-143, doi:10.1016/j.rse.2018.03.017

TABLE OF CONTENTS

Abstract

NASA's Black Marble nighttime lights product suite (VNP46) is available at 15 arc second spatial resolution since January 2012 with data from the Visible Infrared Imaging Radiometer Suite (VIIRS) Day/Night Band (DNB) onboard the Suomi National Polar-orbiting Platform (SNPP). The retrieval algorithm, developed and implemented for routine processing at NASA's Land Science Investigator-led Processing System (SIPS), utilizes all high-quality, cloud-free, atmospheric-, terrain-, vegetation-, snow-, lunar-, and stray light-corrected radiances to estimate daily nighttime lights (NTL) and other intrinsic surface optical properties. Key algorithm enhancements include: (1) lunar irradiance modeling to resolve non-linear changes in phase and libration; (2) vector radiative transfer and lunar bidirectional surface anisotropic reflectance modeling to correct for atmospheric and BRDF effects; (3) geometric-optical and canopy radiative transfer modeling to account for seasonal variations in NTL; and (4) temporal gap-filling to reduce persistent data gaps. Extensive benchmark tests at representative spatial and temporal scales were conducted on the VNP46 time series record to characterize the uncertainties stemming from upstream data sources. Initial validation results are presented together with example case studies illustrating the scientific utility of the products. This includes an evaluation of temporal patterns of NTL dynamics associated with urbanization, socioeconomic variability, cultural characteristics, and settlements for displaced populations affected by conflict. Current and planned activities, under the Group on Earth Observations Human Planet Initiative, are aimed at evaluating the products at different geographic locations and time periods representing the full range of retrieval conditions.

1. INTRODUCTION

1.1.Science/Applications Rationale for the Product

The Day/Night Band (DNB) sensors of the Visible Infrared Imaging Radiometer Suite (VIIRS), on board the Suomi-National Polar-orbiting Partnership (S-NPP) and Joint Polar Satellite System (JPSS) satellite platforms, provide global daily measurements of nocturnal visible and near-infrared (NIR) light that are suitable for earth system science and applications studies. Since the launch of the S-NPP satellite in 2011, multiple studies have used the VIIRS DNB as primary data source covering a wide range of topics such as: (1) feature extraction techniques, based on manual or semi-automated interpretation of the underlying VIIRS DNB radiances, to detect severe weather impacts to urban infrastructure (Cao et al., 2013; Cole et al., 2017; Mann et al., 2016; Molthan and Jedlovec, 2013); (2) detection of sub-pixel scale features, e.g., fires (Polivka et al., 2016), shipping vessels (Asanuma et al., 2016; Elvidge et al., 2015a; Straka et al., 2015), lightning flashes (Bankert et al., 2011), surface oil slicks (Hu et al., 2015), and gas flares (Elvidge et al., 2015b; Liu et al., 2017); and (3) techniques for monitoring nighttime atmospheric optical properties; including clouds (Minnis et al., 2016; Walther et al., 2013), aerosols (Johnson et al., 2013; McHardy et al., 2015), particulate matter (Wang et al., 2016), and gravity waves in the upper atmosphere via nightglow (Miller et al., 2015). Moreover, as with early research that utilized the Defense Meteorological Satellite Program's Operational Line Scanner (DMSP/OLS) (Huang et al., 2014), recent studies using the VIIRS DNB have employed statistical analyses and correlation discovery methods to confirm established empirical relationships with a wide range of human-linked patterns and processes. These include socioeconomic variables (Chen and Nordhaus, 2015; Chen et al., 2015; Levin and Zhang, 2017; Li et al., 2013; Ma et al., 2014; Shi et al., 2014; Yu et al., 2015), as well as changes driven by urban built-up expansion (Guo et al., 2015; Sharma et al., 2016; Shi et al., 2014), energy use (Coscieme et al., 2014; Román and Stokes, 2015), and carbon emissions (Oda et al., 2017; Ou et al., 2015).

In order to make timely and quantitative use of nighttime lights (NTL), one must first quantify the subset of variations that are correlated to human-linked patterns and processes from those that are not. This requirement is especially true for products derived from the VIIRS DNB, given its ultra-sensitivity in low-lit conditions, and the resulting influence of extraneous light emission sources on the NTL time series record. Such artifacts can lead to discrepancies, e.g., when using moon-free NTL composites as proxies to regional-scale socioeconomic features (Bickenbach et al., 2016; Chen and Nordhaus, 2015). To resolve retrieval uncertainties and measurement errors, the quality assurance of NTL products also needs to be emphasized, e.g., by encouraging usage of quality flags that indicate the reliability of individual pixel values, or if retrievals are possibly affected by extraneous artifacts. More broadly, a meta-analysis of 132 research articles revealed the need to better trace the quality and provenance of NTL products as one of the most pressing areas of focus for future studies (Huang et al., 2014).

There is also a need to characterize uncertainties stemming from angular, diurnal, and seasonal variations in atmospheric and surface optical properties. This is crucial since, as we will present in this document, NTL cannot be constrained directly from at-sensor top-of-atmosphere (TOA) radiances in part because of: (1) environmental factors, such as moon light, aerosols, and surface albedo whose reflectance contributes to the observed signal, and (2) errors stemming from seasonal variations and associated surface properties, which can significantly affect estimates of long-term trends. While it is generally neither desirable nor practical to delay the applied use of NTL products until they are proven to be error-free, or until known sources of error have been removed by product reprocessing, it is important to note that space agencies, coordinated by the Committee of Earth Observation Satellites (CEOS), place strong emphasis on product accuracy and performance. This information is needed by decision makers so they can trust the accuracy of the derived products, and by the science community, both to identify poorly performing products and opportunities for improvements, and to draw meaningful inferences from the long-term product records as they relate to trends in human settlements and urbanization.

There is increasing agreement in the growing body of literature concerning factors that govern the utilization of the VIIRS DNB for long-term analyses and near-real time applications. Recent studies have introduced a number of quantitative remote sensing techniques, including: (1) terrain-correction and trending of the VIIRS DNB geolocation (Wolfe et al., 2013); (2) establishing the calibration performance of the VIIRS DNB High Gain Stage (HGS), both in absolute terms and relative to future VIIRS flight units (Lee et al., 2015; Liao et al., 2013; Xiong et al., 2014; Zhang et al., 2016); (3) determining the effective spatial resolution and the impacts of spatial sampling on the VIIRS instrument and higher-level (Level 3) gridded products (Campagnolo et al., 2016; Pahlevan et al., 2017); (4) predicting the DNB's geometric characteristics (i.e., time-varying

Sun/Earth/Moon geometry, moon-illuminated fraction, phase, and albedo) (Miller et al., 2012); (5) estimating the highly variable TOA lunar spectral irradiance (Miller and Turner, 2009); (6) correcting for surface Bidirectional Reflectance Distribution Function (BRDF) effects caused by varying illumination conditions – namely moonlight and reflected airglow from the Earth's upper atmosphere (Cao et al., 2013; Cao and Bai, 2014; Román and Stokes, 2015); and (7) assessing seasonal biases caused by sensor-specific stray light (Lee et al., 2015; Liao et al., 2013; Mills and Miller, 2016), as well as other biogeophysical processes, such as vegetation (Levin, 2017; Levin and Zhang, 2017) and snow cover (Bennett and Smith, 2017).

Despite this progress, substantial gaps remain in the quantification and documentation of uncertainty for NTL data and products. Such information is required by many users, such as the Land Product Validation (LPV) subgroup of the CEOS Working Group on Calibration and Validation (CEOS-WGCV) (Baret et al., 2009; Morisette et al., 2006; Wickland et al., 2014). This development is particularly relevant if these products are to be used to establish global metrics and indicators for achieving a myriad of goals identified under the United Nations Agenda 2030 for Sustainable Development (Griggs et al., 2015). These sustainable development goals (SDGs) include: (1) addressing the needs of conflict-affected populations (SDG-1); (2) quantifying the effectiveness of local electrification projects in the developing world (SDG-7); (3) building resilient infrastructure, promote inclusive and sustainable industrialization and foster innovation; and (4) ensuring that cities and human settlements are inclusive, safe, resilient, and sustainable (SDG-11). While the current Joint Polar Satellite System (JPSS) requirements establish performance metrics for the VIIRS DNB calibration and sensor characteristics, the current DNB-associated key performance requirements are tied strictly to nighttime imagery for short-term operational weather applications at high latitudes (Hillger et al., 2013). Whereas these formalized performance metrics correspond to the "Threshold" requirements of **Table 1**, the "Breakthrough" and "Goal" values point to 1-2 orders of magnitude improvement in sensitivity and spatial resolution. Here, "Threshold" is defined as the minimum requirement to be met to ensure that NTL time series data are useful, and is based on the current JPSS on-orbit performance requirements for the VIIRS DNB's High Gain Stage (HGS) calibration (Liao et al., 2013). The "Goal" is an envisioned ideal requirement above which further improvements are not necessary to achieve all the science and applications underpinning global NTL data products. The "Breakthrough" is an intermediate level between "Threshold" and "Goal", which, if achieved, would result in a significant improvement (WMO, 2016). L_{min} is the minimum detectable NTL radiance and L0 is the robustness or uncertainty (standard deviation) with respect to L_{min}. All values in **Table 1** pertain to Land-based NTL detections.

Table 1 Key performance metrics established for NASA's Black Marble product suite.

Key Performance Metrics	Threshold	Breakthrough	Goal
NTL Detection Limit (L_{min})	3.0 $nW \cdot cm^{-2} \cdot sr^{-1}$	0.5 $nW \cdot cm^{-2} \cdot sr^{-1}$	0.25 $nW \cdot cm^{-2} \cdot sr^{-1}$
NTL Robustness (L_0)	± 3.0 $nW \cdot cm^{-2} \cdot sr^{-1}$	± 0.10 $nW \cdot cm^{-2} \cdot sr^{-1}$	± 0.05 $nW \cdot cm^{-2} \cdot sr^{-1}$
Stray Light Error	0.45 $nW \cdot cm^{-2} \cdot sr^{-1}$	0.25 $nW \cdot cm^{-2} \cdot sr^{-1}$	< 0.1 $nW \cdot cm^{-2} \cdot sr^{-1}$
Spatial Resolution	742 m (±5%)	500 m (±5%)	≤ 200 m (±5%)
Temporal Resolution	Monthly	Daily	Hourly
Geolocation Uncertainty	133 m	50 m	20 m

1.2. Intended User Community

The communities, who have been using the Black Mable product, include, but are not limited to:

- Disaster risk reduction
- Urban land cover/land use change and sustainability
- Socioeconomic factors and demographic changes
- Regional conflict monitoring
- Global and regional climate modeling communities
- Ocean ecosystems and sustainable fisheries
- Light pollution studies

2. THE ALGORITHM

2.1. Algorithm Description

The operational NASA Black Marble product suite (VNP46) ingests multiple source datasets and ancillary data to output the highest quality pixel-based estimates of NTL. These NTL estimates are accompanied by pixel-level quality flags. The principal features of the algorithm are illustrated in **Figure 2**, and are summarized in the following sections.

2.1.1. Atmospheric Correction

NASA's Black Marble retrieval strategy combines daytime VIIRS DNB surface reflectance, Bidirectional Reflectance Distribution Function (BRDF), Surface Albedo, Nadir BRDF-Adjusted Reflectance (NBAR), and Lunar irradiance values to minimize the biases caused by extraneous artifacts in the VIIRS NTL time series record.

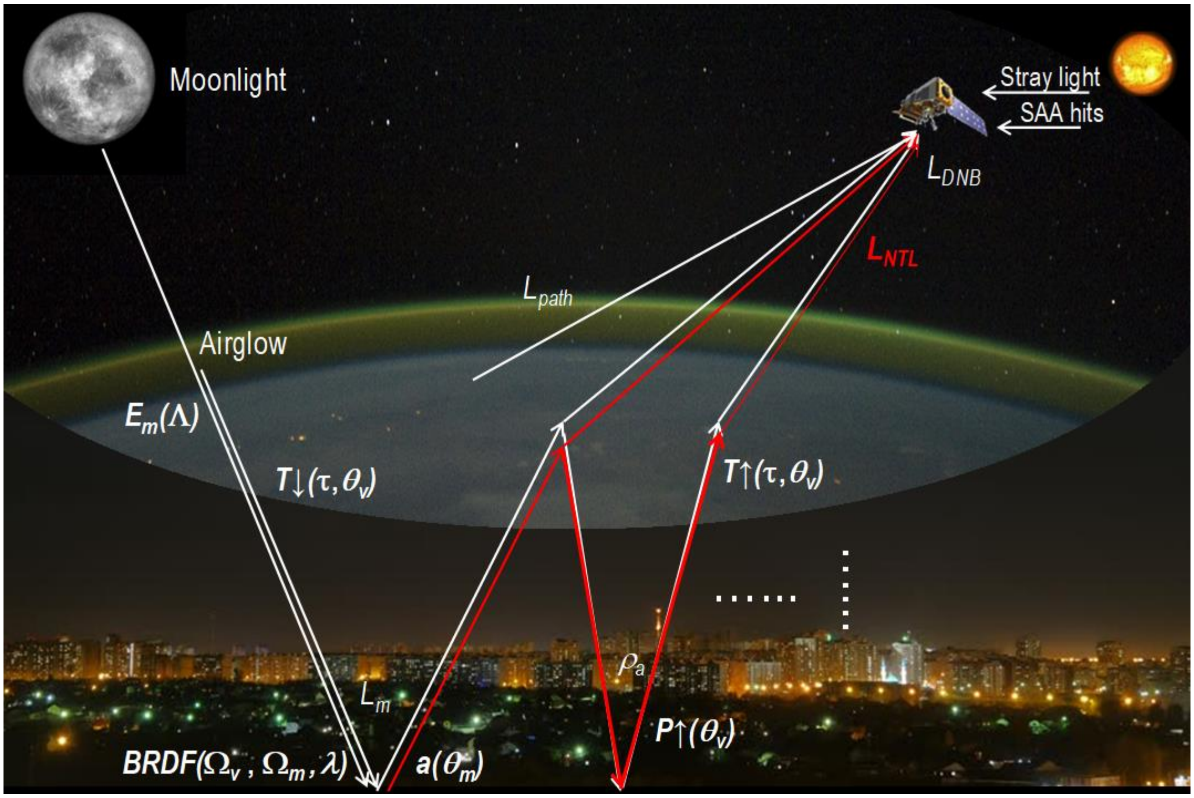

Figure 1 Overview of NASA's Black Marble retrieval strategy (cf., Equation 1). During the ~50% portion of the lunar cycle when moonlight is present at the time of satellite observation, the surface upward radiance from artificial light emissions, L_{NTL} [units of nWatts·cm^{-2}·sr^{-1}], can be extracted from at-sensor nighttime radiances at TOA, L_{DNB}. L_{path} is the nighttime path radiance, $a(\theta_m)$ is the VIIRS-derived actual surface albedo. The atmospheric backscatter is given by ρ_a. $T\downarrow(\tau,\theta_v)$ and $T\uparrow(\tau,\theta_v)$ are the total transmittances along the lunar-ground and ground-sensor paths (respectively). $P\uparrow(\theta_v)$ is the probability of the upward transmission of NTL emissions through the urban vegetation canopy. Additional factors accounted for in the Level 1 process (Section 3.1) include correction for straylight and South Atlantic Anomaly (SAA) hits.

Using this novel "turning off the Moon" approach, illustrated in **Figure 1**, the surface upward radiance from artificial light emissions, L_{NTL} [units of nWatts·cm^{-2}·sr^{-1}], can be extracted from at-sensor nighttime radiances at TOA, L_{DNB}, using the following equation:

$$L_{NTL} = \left[\left(\frac{L_{DNB} - L_{path}}{T_{\uparrow}(\tau, \theta_v)} \right) (1 - a(\theta_m)\rho_a) - (L_m T_{\downarrow}(\tau, \theta_m) a(\theta_m)) \right] \Big/ P_{\uparrow}(\theta_v) \qquad (1)$$

where L_{path} is the nighttime path radiance (*i.e.*, the radiance generated by scattering within the atmosphere), and $a(\theta_m)$ is the VIIRS-derived actual (or Blue-Sky) surface albedo; incorporating the directional influence of sky radiance and multiple scattering effects between the ground and the atmosphere (Román et al., 2010). For the latter, a separate snow albedo retrieval scheme is used if the VIIRS current day snow status flag is activated (Klein and Stroeve, 2002; Y. Liu et al., 2017; Moustafa et al., 2017; Wang et al., 2012). $P\uparrow(\theta_v)$ is defined in Equation 10 (see Section 2.3 for details). The atmospheric backscatter is given by ρ_a, and $T\downarrow(\tau,\theta_v)$ and $T\uparrow(\tau,\theta_v)$ are the total transmittances (including direct and diffuse radiation) along the lunar-ground and ground-sensor paths (respectively). The latter two are a function of view-illumination geometry and the total atmospheric column optical depth (τ) due to mixed gases, water vapor, and aerosol particles. The retrieval uses a modified algorithm based on the heritage VIIRS Surface Reflectance Intermediate Product (IP) to estimate the values of L_{path}, ρ_a, $T\downarrow(\tau,\theta_v)$, and $T\uparrow(\tau,\theta_v)$ for a given set of surface and atmospheric conditions (Roger et al., 2016; Skakun et al., 2018). Additional input datasets include the standard VIIRS Cloud Mask (VCM) (Kopp et al., 2014), atmospheric profiles obtained from National Centers for Environmental Prediction (NCEP) model inputs (*i.e.*, water vapor, ozone, and surface pressure) (Moorthi et al., 2001), and the VIIRS aerosol model combined with daytime-to-daytime averaged Aerosol Optical Depth (AOD 0.550μm) to extrapolate the nighttime AOD (Vermote et al., 2014).

2.1.2. BRDF Correction

The surface Bidirectional Reflectance Distribution Function (BRDF, or reflectance anisotropy) is governed by the angle and intensity of illumination – whether that illumination be solar or lunar or from airglow emissions – and by the structural complexity of the surface, resulting in variations in brightly illuminated regions and darkly shadowed areas. The semi-empirical RossThick-LiSparse Reciprocal (RTLSR, or Ross-Li) BRDF model (Román et al., 2010; Roujean et al., 1992; Schaaf et al., 2011a, 2002; Strahler et al., 1999) is advantageous in this regard, since (1) it is the most likely kernel-driven combination to capture the wide range of conditions affecting the VIIRS DNB on a global basis; (2) it allows analytical model inversion with a pixel-specific estimate of uncertainty in the model parameters and linear combinations thereof (Lucht and Roujean, 2000); and (3) the scheme is flexible enough that other kernels can be easily adopted should any become available and should they be shown to be superior for a particular scenario.

For VIIRS DNB acquisitions over snow-free and snow-covered surfaces, we define the spectral radiance contribution from moonlight, L_m,

$$L_m(\Omega_v, \Omega_m, \Lambda) = \frac{E_m(\Lambda)}{\pi} BRF(\Omega_v, \Omega_m, \Lambda)\cos(\theta_m) \tag{2}$$

in terms of the Ross-Li model:

$$BRDF(\Omega_v, \Omega_m, \lambda) \cong BRF(\Omega_v, \Omega_m, \Lambda) = f_{iso}(\Lambda) + f_{vol}(\Lambda) K_{vol}(\Omega_v, \Omega_m) + f_{geo}(\Lambda) K_{geo}(\Omega_v, \Omega_m) \tag{3}$$

$$K_{vol} = \frac{(\pi/2 - \xi)\cos\xi + \sin\xi}{\cos\theta_m + \cos\theta_v} - \frac{\pi}{4} \tag{4}$$

$$\cos\xi = \cos\theta_m \cos\theta_v + \sin\theta_m \sin\theta_v \cos\Delta\phi \tag{5}$$

$$K_{geo} = \frac{1 + \sec\theta'_m \sec\theta'_v + \tan\theta'_m \tan\theta'_v \cos\Delta\phi}{2} + \left(\frac{t - \sin t \cos t}{\pi} - 1\right)\left(\sec\theta'_m + \sec\theta'_v\right) \tag{6}$$

$$\cos^2 t = \min\left\{\left(\frac{P_4}{\sec\theta'_v + \sec\theta'_m}\right)^2 \left[D^2 + \left(\tan\theta'_v \tan\theta'_m \sin\Delta\phi\right)^2\right],\ 1\right\} \tag{7}$$

$$\tan\theta'_x = P_5 \tan\theta_x \quad ; \; x = v \;\; or \;\; s \tag{8}$$

$$D = \sqrt{\tan^2\theta'_m \tan^2\theta'_v - 2\tan\theta'_m \tan\theta'_v \cos\Delta\phi} \tag{9}$$

Here, we define the wavelength for the narrowband instrument of interest as the weighted center, Λ, of the VIIRS DNB spectral band [0.5 - 0.9 μm]. Parameter $f_{iso}(\Lambda)$ is the isotropic scattering component and equal to the bidirectional reflectance for a pixel viewing zenith angle $\theta_v = 0$ and a lunar zenith angle $\theta_m = 0$. Parameter $f_{geo}(\Lambda)$ is the coefficient of the LiSparse-Reciprocal geometric scattering kernel K_{geo}, derived for a sparse ensemble of surface casting shadows on a Lambertian background (Li and Strahler, 1992). Parameter $f_{vol}(\Lambda)$ is the coefficient for the RossThick volume scattering kernel K_{vol}, so called for its assumption of a dense leaf canopy (Ross, 1981). $\Delta\phi$ is the relative view-sun azimuth angle ($\Delta\phi = \phi_m - \phi_v$) and ξ is the scattering phase angle between moon and view directions. The two constants, dimensionless crown relative height ($P_4 = h / b$) and shape ($P_5 = b / r$) parameters, have been fixed at $h / b = 2$ and $b / r = 1$ to invert the angular radiance data from the VIIRS DNB (Wanner et al. 1997). For these two parameters, h is the variable for height at which a crown center is located, b is the vertical half axis of the modeled ellipsoid, and r is its horizontal radius. E_m (Λ) [units of $nW \cdot m^{-2}$] is the downwelling TOA sensor response function-weighted lunar irradiance (Miller and Turner, 2009), and *BRF* is the surface bidirectional reflectance factor – the ratio of the BRDF to that of a perfect Lambertian reflector (*i.e.*, BRF $\approx$ πBRDF) (Nicodemus, 1977; Schaepman-Strub et al., 2006).

To achieve a high-quality BRDF retrieval, the NASA Black Marble algorithm collects all available daytime, atmospherically-corrected, VIIRS DNB BRFs over a multi-date period (normally 16-days) to establish the analytical solution for the Ross-Li BRDF model parameter values, $f_k(\Lambda)$. Note that during moon-free nights when atmospheric air glow is the dominant emission source, the VNP46 algorithm sets the illumination geometry to near-nadir (θ_m = 10°) and the Lunar Irradiance to E_m (Λ) = 0.52 $nW \cdot m^{-2}$ (Liao et al., 2013). This enables a BRDF correction even in the absence of moonlight.

2.1.3. Seasonal Vegetation Correction

Another known source of uncertainty in the retrieval of satellite-derived NTL is the influence of canopy-level foliage along the ground-to-sensor geometry path (Román and Stokes, 2015). This effect, which has been shown to reduce the magnitude of NTL at city-wide scales (Levin, 2017; Levin and Zhang, 2017), is most pronounced in temperate urban regions; where mixed and deciduous vegetation are most pervasive. Given its seasonal dependence, this occlusion effect (obscuration of surface light by foliage) should be proportional in magnitude to the density and vertical distribution pattern of leaves within a given VIIRS DNB pixel. Hence, while the effect may be non-linear (due to the confluence of factors that control the seasonality, physiognomy, and vertical distribution of urban vegetation canopies), the effect can be parameterized using analytical models which aim to retrieve canopy structure parameters from multi-angle remote sensing data (Chopping, 2006). With this concept in mind, we are employing a vegetation dispersion parameter, known as the clumping index, ψ, to parameterize the confined distribution of foliage within distinct canopy structures (Chen et al., 2005; Chen and Black, 1991; Leblanc et al., 2005; Nilson, 1971):

$$P_{\uparrow}(\theta_v) = e^{-\psi G(\theta_v) LAI / cos(\theta_v)} \qquad \textbf{(10)}$$

Here, $P\uparrow(\theta_v)$ is the probability of the upward transmission of NTL emissions through the urban vegetation canopy (known as the gap fraction probability and hereafter termed the P_{gap} equation), $G(\theta_v)$ is the extinction coefficient that expresses the mean area projection of plant elements in the direction θ_v (being 0.5 for canopies with a random distribution of leaf angles), and *LAI* is the Leaf Area Index. If $LAI = 0$, then $P\uparrow(\theta_v) = 1$ and a correction is not performed. When $LAI > 0$, and foliage grouping has a random distribution, then the clumping index $\psi = 1$ and Equation 10 returns to the original Beer's law. The latter includes areas with single ground-layers (*e.g.*, peri-urban vegetation). Conversely, if the distribution is not random, then the clumping index can be larger or smaller than unity. In the case that the leaf distribution is more regular (leaves side by side) than random, then the clumping index $\psi > 1$. As such, the same value of *LAI* over a given VNP46 pixel, can intercept more NTL emissions originating from the ground surface; thus, making $P\uparrow(\theta_v)$ smaller, and the corresponding adjustment to L_{NTL} ($P\uparrow(\theta_v)$ in Equation 1) is larger.

The P_{gap} equation can be inverted from available daily VIIRS BRDF-derived clumping index values, as done in *Hill et al.*, (2011) and *He et al.*, (2012). The VIIRS LAI retrievals are based on the current standard product (Park et al., 2017). In the case of poor-quality or missing LAI values (*e.g.*, when LAI is not retrieved over dense urban areas), we are employing the VIIRS LAI backup algorithm by using a Look-up Table (LUT) (Knyazikhin et al., 1999; Xiao et al., 2016) with Normalized Difference Vegetation Index (NDVI) generated from high quality retrievals from the VIIRS NBAR product (Shuai et al., 2013). Using this approach, we can define the clumping index based on Chen et al., (2005) as:

$$\psi = C(\theta_v) NDHD(\Omega_v, \Omega_m, \Lambda) + D(\theta_v) \qquad \textbf{(11)}$$

$$NDHD(\Omega_v, \Omega_m, \Lambda) = \frac{BRF_{hot}(\Omega_v, \Omega_m, \Lambda) - BRF_{dark}(\Omega_v, \Omega_m, \Lambda)}{BRF_{hot}(\Omega_v, \Omega_m, \Lambda) + BRF_{dark}(\Omega_v, \Omega_m, \Lambda)} \qquad \textbf{(12)}$$

Here, *NDHD* is the Normalized Difference between Hotspot and Darkspot (NDHD) – an angular index used to characterize the anisotropic behavior of vegetation, which has been related to ground based measurements of clumping index (He et al., 2012; Lacaze et al., 2002; Leblanc et al., 2005; Zhao et al., 2012). BRF_{hot} and BRF_{dark} are the reflectances at the 'hotspot' and 'darkspot', respectively. Thus, NDHD can be estimated directly from the retrieved VIIRS BRDF model parameters (f_{iso}, f_{vol}, f_{geo} in Equation 3) by specifying the RTLSR model kernels for the corresponding hotspot and darkspot geometries. The values of $C(\theta_v)$ and $D(\theta_v)$ in Equation 11 are estimated by applying the linear coefficients of the line of best fit to the VIIRS-derived NDHD values (see Table 2 in Chen et al., 2005). For the VNP46 implementation, we chose the coefficients of regression based on a full ellipsoid shape in the Red spectral region [0.662 - 0.682 μm]. The P_{gap} effect is dominant across NTL pixels with lower build-up densities (*e.g.*, small cities and suburban areas), where green spaces are often protected from development. In contrast, P_{gap} values are often closer to unity (no correction) near densely-built city centers (e.g. Paris and Chicago).

2.2. Product Description

The NASA Black Marble product suite includes daily at-sensor TOA nighttime radiances (VNP46A1) and daily moonlight and atmosphere corrected NTL (VNP46A2) products at 15 arc second geographic Linear Lat/Lon grid. The data are available in standard land HDF-EOS (Hierarchical Data Format - Earth Observing System) format. The VNP46A1 product contains 26 layers including sensor radiance, zenith and azimuth angles at sensor, solar, and lunar, cloud mask flag, time, shortwave IR radiance, brightness temperatures, VIIRS quality flags, moon phase angle, and moon illumination fraction. The detail information on these VNP46A1 product layers is given in

Table *7*. The VNP46A2 products has 7 layers containing information on BRDF-corrected NTL, Gap-filled BRDF-corrected NTL, lunar irradiance, mandatory quality flag, high quality retrieval (number of days), snow flag, and cloud mask flag. The detail VNP46A2 layer properties are described in **Table 8**. These data will be made available both retrospectively, via NASA's Level 1 and Atmosphere Archive and Distribution System (LAADS), and in forward (near-real time) data streams, via NASA's Land, Atmosphere Near Real-time Capability for EOS (LANCE).

3. PRODUCT GENERATION

3.1. Level 1 calibrated DNB radiances

The VIIRS DNB sensor is a temperature controlled Charge Coupled Device (CCD) that has 672 sub-pixel detectors along-track, which are aggregated on-board to create 16 nearly constant 742 m along-track pixels for each along-scan frame (Wolfe et al., 2013). These observations are acquired at three different stages of Low- Mid- and High Gain (LGS, MGS, and HGS, respectively) with high sensitivity for low NTL conditions (Mills and Miller, 2016). With the aggregation mode, detector, gain stage, and Half-angle Mirror (HAM)-side dependent calibration performed, the VIIRS DNB degradation was conclusively traced and has been well characterized (Chen et al., 2017; Xiong et al., 2014). The stray light contamination on the DNB, which is a transient issue affecting up to 25% of night scenes in the mid-to-high latitude regions (Chen et al., 2017; Mills et al., 2013), is also being routinely corrected by the VIIRS Calibration Support Team (VCST) (Chen et al., 2017; Lee et al., 2014). Results from ongoing Collection V001 reprocessing of the NASA Level 1 product includes additional updates to the VIIRS DNB terrain-corrected geolocation, straylight, and calibration LUTs. Finally, routine reporting and removal of bad DNB granules (e.g., resulting from Suomi-NPP calibration maneuvers or Rotating Telescope Assembly (RTA)/HAM sync loses) is being conducted by the VIIRS Calibration Support Team (VCST) using specialized software to mitigate leakage into the VNP46 product suite.

3.2. Algorithm Processing Cycle

NASA's Black Marble (VNP46) algorithm processing cycle is divided into daytime and nighttime branches (**Figure 2**). Each processing branch produces a unique set of ancillary and quality assurance (QA) flags.

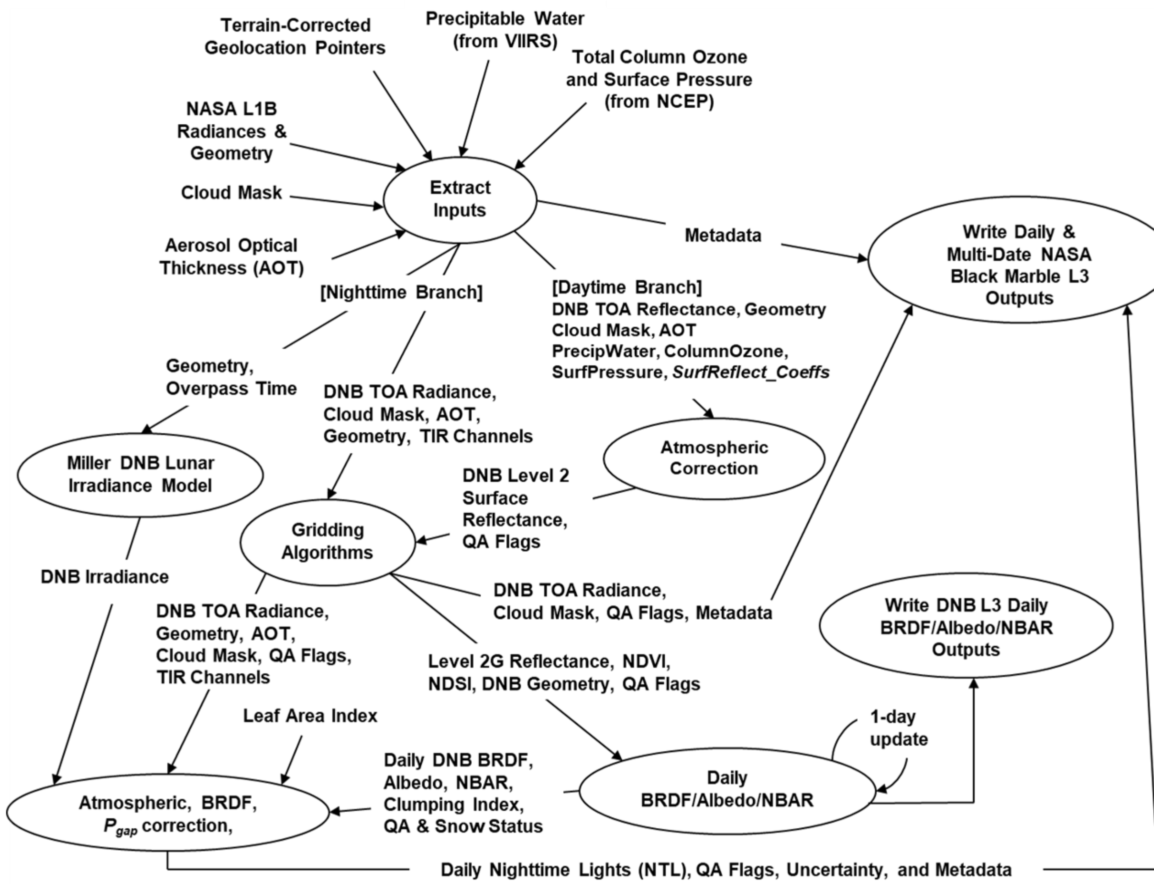

Figure 2 Algorithm processing cycle and ancillary parameters used by NASA's Black Marble product suite (VNP46).

For the daytime branch, science processing software based on the standard suite of VIIRS Land products are integrated as part of NASA's Black Marble processing chain. First, a modified version of the operational VIIRS Surface Reflectance algorithm (Roger et al., 2016; Vermote et al., 2014) is used to generate the DNB surface bi-directional reflectances (BRFs) using NASA's Level 1B calibrated radiance product as input (i.e., 6-minute granules, or 2366 km along track and ~3100 km across-track). Level 2G DNB Surface Reflectances are then generated by performing spatial and temporal aggregation to 15 arc second grid cells over daily time periods (Campagnolo et al., 2016; Pahlevan et al., 2017; Wolfe et al., 1998; Yang and Wolfe, 2001). Daily Level 3 DNB BRDF/Albedo data are then retrieved using the VIIRS heritage algorithm (VNP43) (Liu et al., 2017), and corresponding Snow Flags are estimated using the heritage VIIRS Normalized Difference Snow Index (NDSI) algorithm (VNP10) (Riggs et al., 2017, 2016). The NDVI and NDSI values are used to determine the growing, dormant, and snow periods to update the *a priori* global database of the DNB BRDF product (Cescatti et al., 2012; Y. Liu et al., 2017; Román et al., 2009). Surface BRFs from the VIIRS I1 (red) and I2 (NIR) channels are used to obtain daily estimates of LAI (Knyazikhin et al., 1999; Park et al., 2017; Xiao et al., 2016). The retrieved LAI and clumping index values are then used to calculate the gap fraction probability (P_{gap}).

The nighttime branch describes the path followed to generate the final VNP46 products. We begin with the at-sensor TOA nighttime radiances (VNP46A1), along with the corresponding nighttime cloud mask, multiple Solar/Viewing/Lunar geometry values (including moon-illuminated fraction and phase angles), and the daily snow and aerosol status flags. These additional Science Data Sets (SDS) enable open access to the primary inputs used to generate the NASA Black Marble NTL time series record; thus, ensuring reproducibility of the final outputs. For example, using VNP46A1 as input, end-users seeking to employ NTL data in light pollution studies can develop different variations of the products under different sky-illumination conditions (e.g., daily retrievals in which atmospheric, topographic and cloud effects are removed, but seasonal and lunar-related changes are not removed). Algorithm developers also interested in contributing additional refinements to the VNP46 product suite, or in developing their own series of higher-level DNB products (*e.g.*, for nighttime aerosol, cloud optical properties, and ocean NTL applications), can also make use of these SDS layers; thus, greatly reducing the complexity of data processing and subsequent analyses. A series of temporal and spatial gap-filling techniques are also employed to improve the coverage of the VNP46 NTL product.

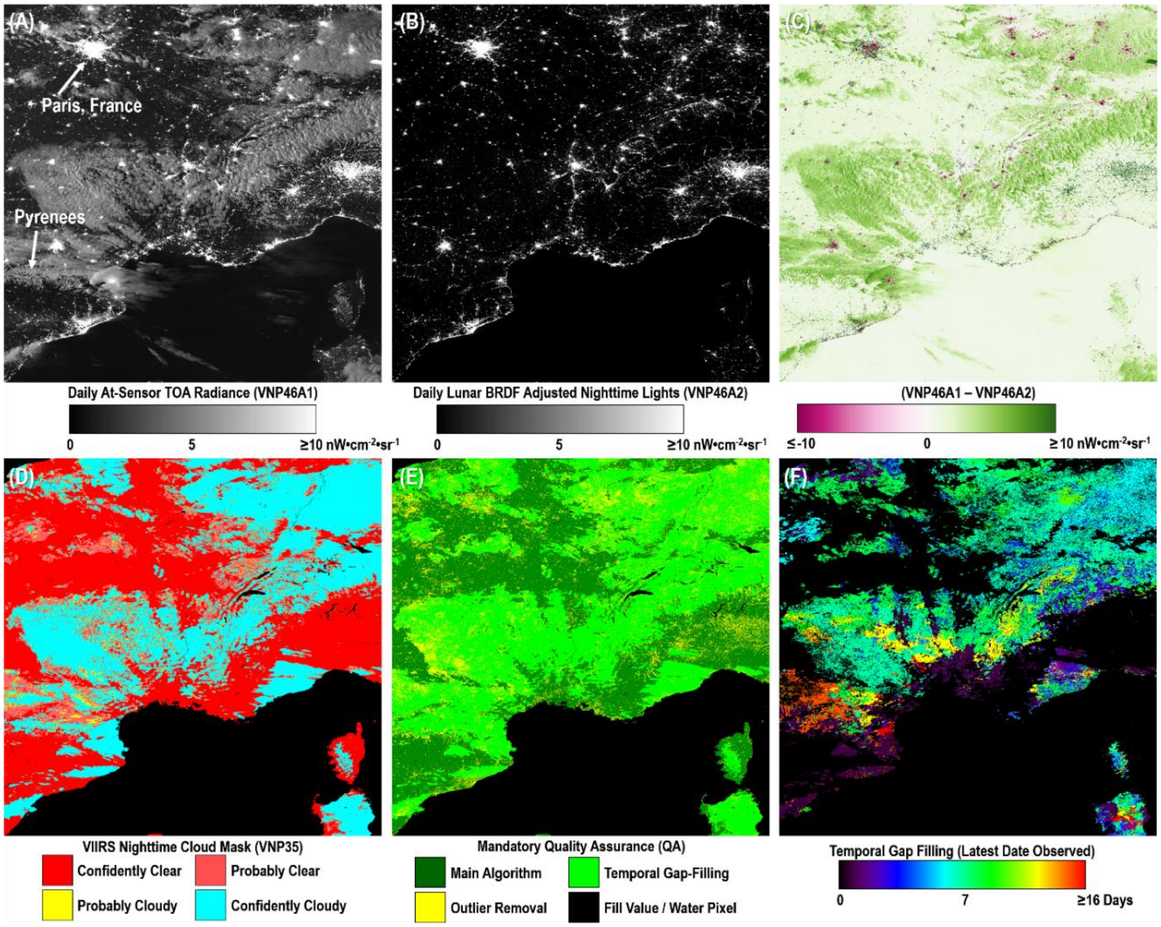

Figure 3 VNP46 product suite components for a 10° x 10° Level 3 tile over France and the Balearic Sea region (h18v04; DOY 2015-091). The full-moon-illuminated and 51% cloud-contaminated scene illustrates the challenges of nighttime cloud-masking over snow- covered surfaces (e.g., the French Alps and the Pyrenees).

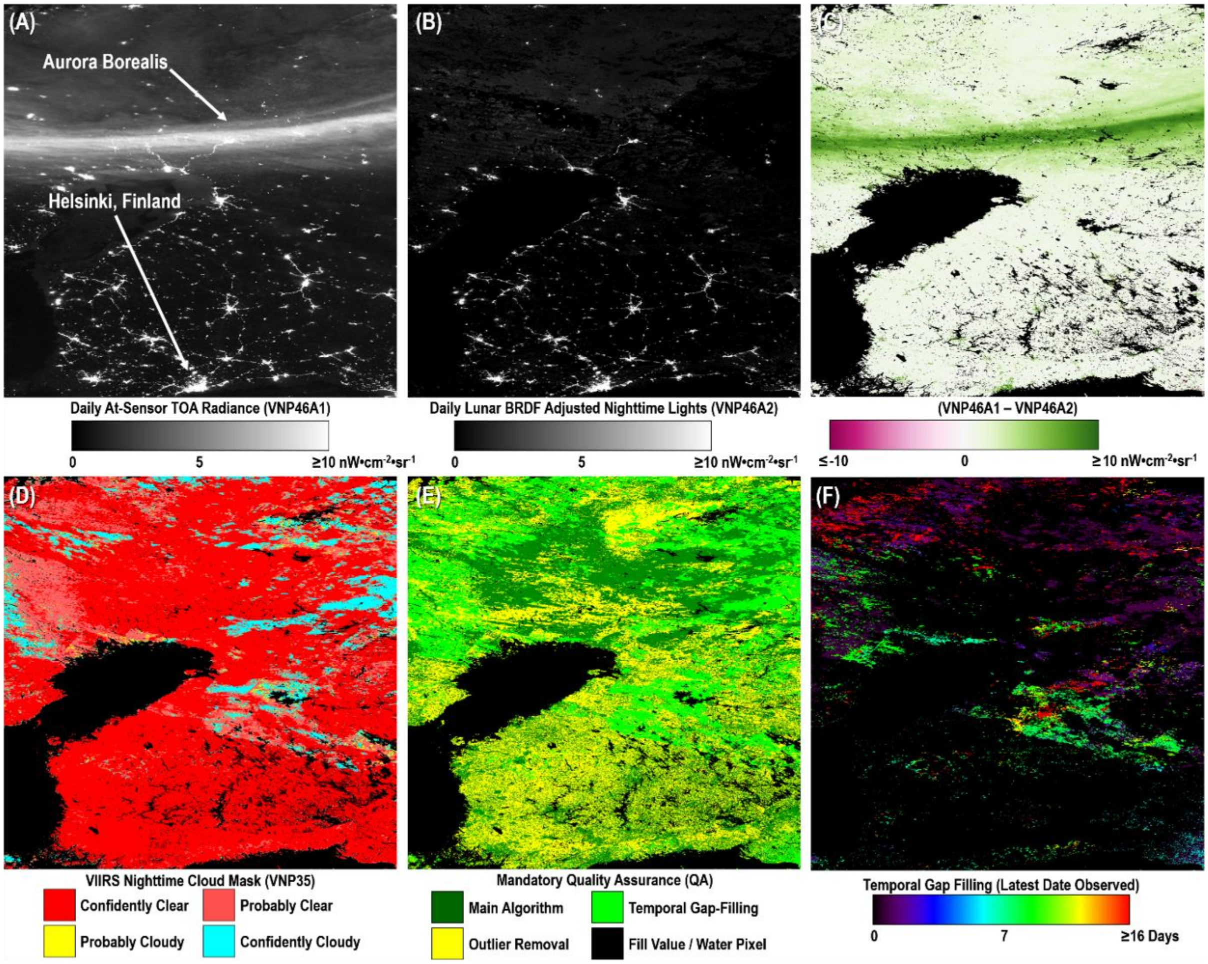

Figure 4 VNP46 product suite components for a 10° x 10° Level 3 tile over Sweden and Finland (h20v02; DOY 2013-080). The half-moon-illuminated and 30% cloud-contaminated scene is shown to capture extraneous light emissions north of the Gulf of Bothnia caused by the Aurora Borealis.

Results shown in **Figure 3** and **Figure 4** illustrate the key processing steps used to retrieve high-quality NTL as part of NASA's Black Marble product suite. Cloud-free, atmospheric-, seasonal-, and moonlight BRDF-corrected DNB nighttime radiances are produced using the nighttime DNB Level 1 at-sensor radiances, nighttime cloud mask, aerosol optical depth values, snow status flag, Ross-Li DNB BRDF model parameters and albedo values, P_{gap}, and per-pixel estimates of DNB Lunar irradiance and corresponding geometries. A mandatory quality assurance (QA) flag is then provided to establish the pixel-specific estimates of retrieval performance. Note that, when the temporal gap-filling routine is called upon, as reported in the Mandatory Quality Assurance (QA) Flags (**Table 10**), the latest high-quality date observed, based on retrievals using the main algorithm, is reported as a separate SDS layer. If an outlier is still detected, after temporal gap-filling, then the VNP46 algorithm defaults to a monthly climatology based on the most recent available moonless high QA values. Thus, through judicious use of the VNPD46 product quality flag, the end-user can establish whether a particular temporally-gap filled NTL value is based on a recent date or not. This results in a traceable moonlight-adjusted NTL product to assess current versus recent NTL conditions, while reducing persistent data gaps caused by nighttime clouds, snow, and other ephemeral artifacts (*e.g.*, the Aurora Borealis - *cf*., **Figure 4**). The reader is referred to the Appendix for additional details regarding the individual VNP46 products, including a full description of quality flags and controls exercised through the NTL retrieval process.

4. PRODUCT ACCURACY/UNCERTAINTY

4.1. Evaluation of Product Performance

The overarching goal of NASA's Black Marble science product development efforts is to achieve a "Breakthrough" performance specification (*cf.*, **Table 1**) by conducting the following tasks: (1) long-term stability monitoring of the entire VNP46 algorithm processing chain, including the fundamental (Level 1B) VIIRS DNB time series record, terrain-corrected geolocation, straylight correction, and calibration LUTs; and (2) global quality assessment, uncertainty quantification, and product validation. To assess progress on these tasks, we have developed a series of seven benchmark tests to quantify product performance at representative spatial and temporal scales. This comprehensive suite of benchmark tests and assessment metrics is meant to ensure that variations in VNP46 product performance can be identified quickly, so that improvements can be implemented in a timely fashion. It also enables the end-user to consider the products in their appropriate context, *e.g.*, by anticipating appropriate noise reduction levels under specific retrieval conditions.

4.1.1. Detection Limit and Robustness

To enable quantitative uses of NTL time series data, one must first establish the robustness of the algorithm with appropriate detection limits that are globally applicable and temporally consistent. This is particularly true when using NTL to characterize abrupt short-term changes (*e.g.*, power outages) or to quantify low-lit NTL across areas of concentrated energy poverty. Accordingly, we conducted a series of benchmark tests to address the following questions:

– **Benchmark Test #1:** How do daily variations in aerosol optical depth, under varying view-illumination conditions, influence NTL retrieval performance?

– **Benchmark Test #2:** How do daily variations in surface albedo, under varying view-illumination conditions, influence NTL retrieval performance?

– **Benchmark Test #3:** Is there a dependence between NTL and daily variations in anisotropic diffuse moon-illumination and multiple scattering (i.e., Albedo-aerosol coupling effects)?

The goal of benchmark tests #1 to #3 is to assess variations in low-lit NTL emissions; hereby expressed in terms of the background noise, or floor, of a NTL product; where both L_{min} and L_0 should equal to 0.0 $nW \cdot cm^{-2} \cdot sr^{-1}$. For each benchmark test, we employed a large spatial sample of 30 Level 3 tiles (each sized: 10° x 10° - *cf*., highlighted red tiles in **Figure 12**) using the entire available VIIRS DNB (Collection V001) time series. This augmented analysis was necessary to capture a diverse range of geographic locations and time periods representing global conditions. To further establish whether a correction resulted in improved performance, each benchmark test was conducted at two different levels of the NASA Black Marble algorithm processing chain: (1) at the upstream level, using cloud-corrected at-sensor TOA radiances only (hereby termed, TOA), and (2) at the final processing level; using cloud-, atmospheric-, seasonal-, and moonlight BRDF-corrected NTL data (VNP46A2).

We used the following sampling scheme to produce statistical metrics for each benchmark test: (1) Background NTL pixels contained within each sampled Level 3 tile (30 in total) were identified using the Global Urban Footprint (GUF) product (Esch et al., 2017, 2013) and removing 1% of outliers. (2) The samples were partitioned into 12 groupings, each representing a discrete range of daily black-sky albedo (BSA, BSA < 0.2, BSA ≥ 0.2), viewer zenith angle (VZA, VZA < 45°, VZA ≥ 45°), and aerosol optical depths (AOD, AOD < 0.5, AOD ≥ 0.5) (see plot legends in **Figure 5-Figure 10**). (3) For each of these groupings, the average TOA and VNP46A2 radiance was estimated for instances with matching illumination conditions. (4) Finally, each of these instances was then paired with sample data from the entire available DNB time series record (2012-mid 2017), corresponding to the full range of illumination conditions (i.e., average values for samples with moon illuminated fractions from 0% to 100%, with a precision of ±1.5°). Results for benchmark tests #1 to #3 (**Figure 5-Figure 10**), as well as summary statistics extracted for four final groupings (i.e., TOA vs VNP46A2, for moon illuminated fraction < 50% and moon illuminated fraction ≥ 50%) (**Table 2-Table 4**), illustrate the highly non-linear dependence of background DNB pixels to BSA, VZA, AOD, and combinations thereof.

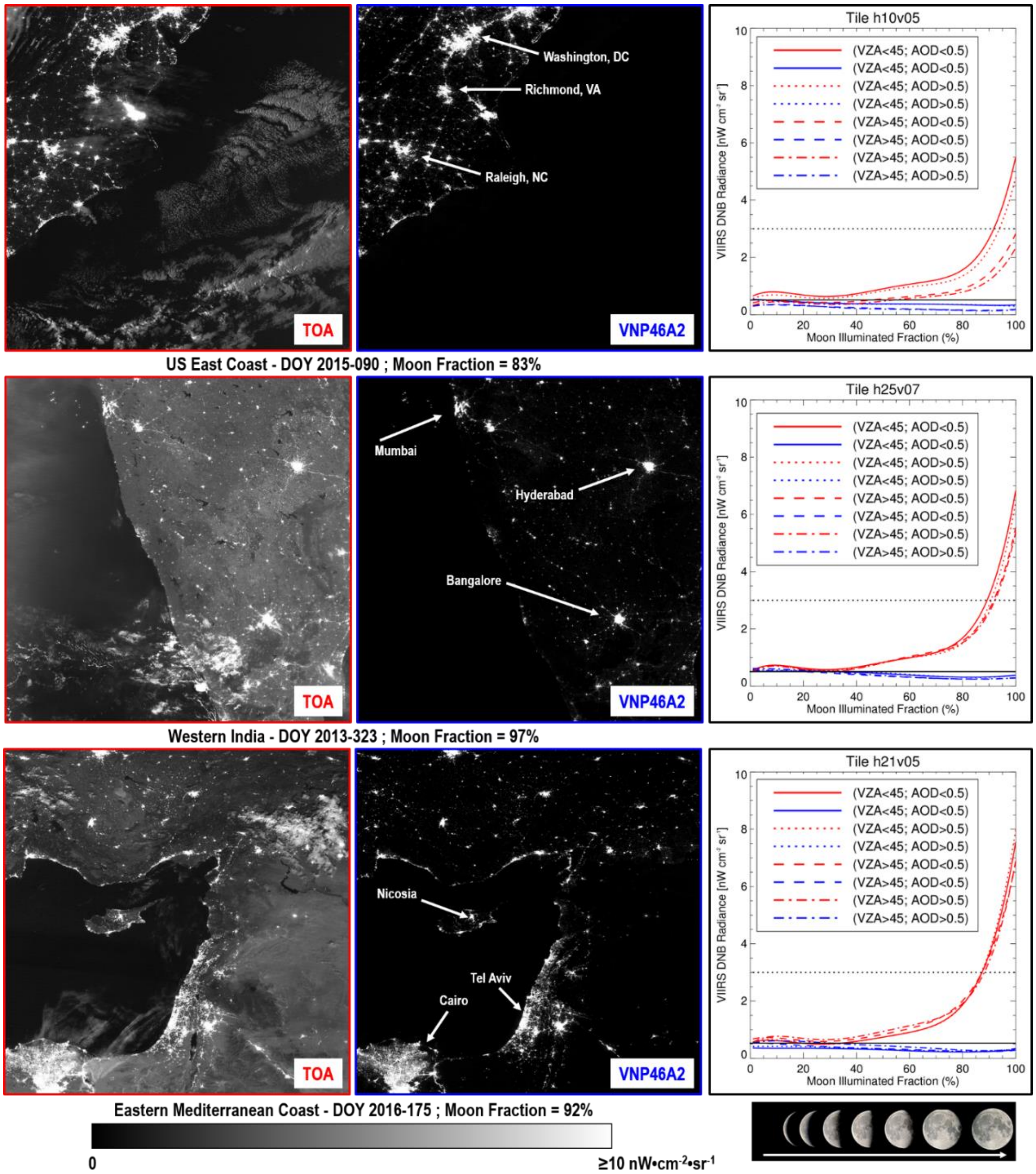

Figure 5 Benchmark Test #1: NTL (View Zenith Angle (VZA), Aerosol Optical Depth (AOD). (Left and Center) Daily VIIRS TOA (cloud-corrected at-sensor DNB radiances in nW·cm^{-2}·sr^{-1}) and VNP46A2 scenes (cloud-free, atmospheric-, seasonal-, and moonlight BRDF-corrected DNB nighttime radiances) are shown in red and blue (respectively) for three Level 3 tiles exhibiting near- to full- moon conditions. Cloudy pixels were left visible in the TOA product for viewing purposes. (Right) Benchmark Test #1 plots corresponding to each scene. For reference, the

threshold (L_{min} = 3.0 nW·cm^{-2}·sr^{-1}) and breakthrough (L_{min} = 0.5 nW·cm^{-2}·sr^{-1}) performance specifications are shown as black-dotted and solid horizontal lines (respectively).

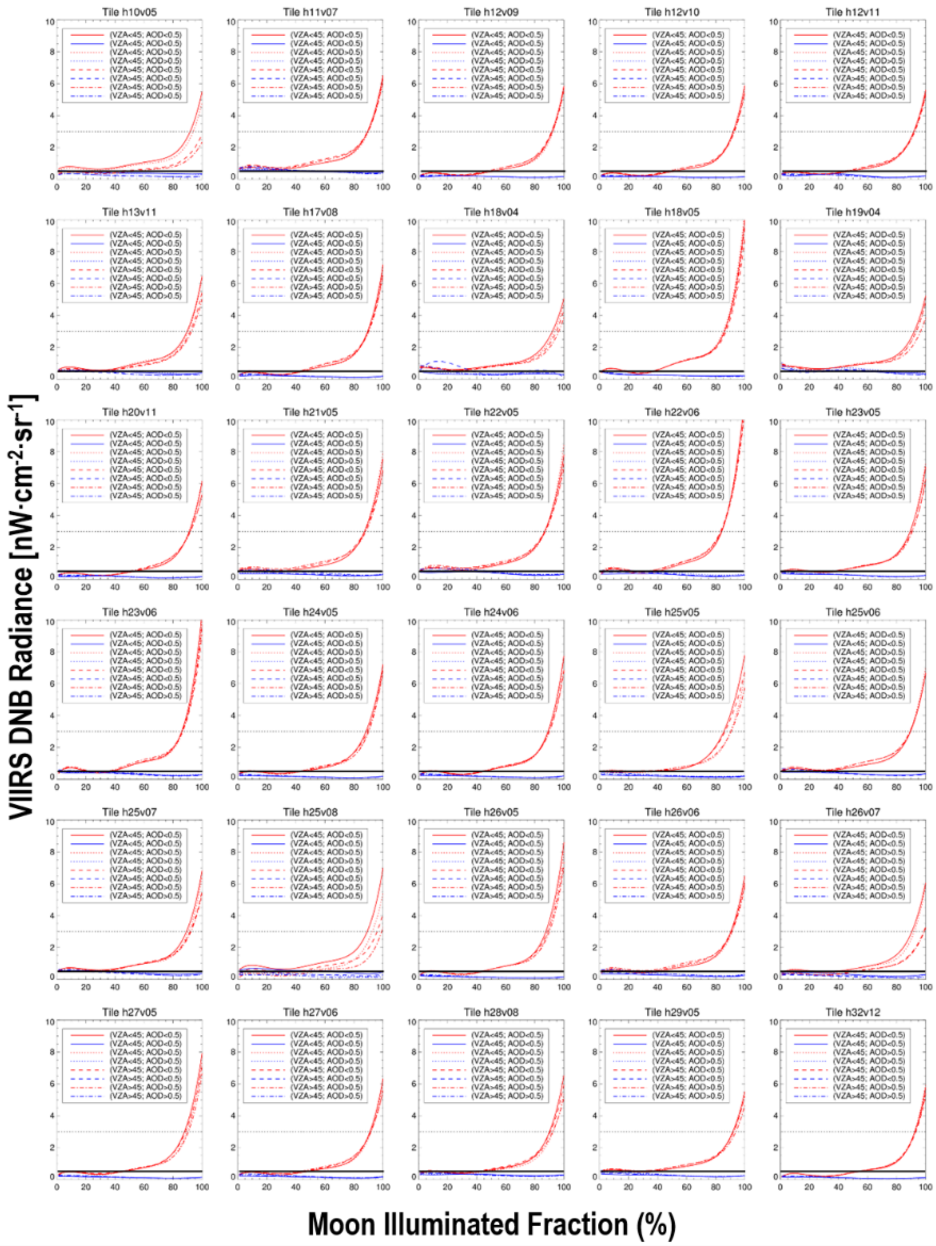

Figure 6 Results for Benchmark Test #1: NTL (VZA, AOD). A globally representative spatial sample of 30 VIIRS Level 3 tiles provides insights into the performance of the NASA Black Marble NTL radiance product (VNP46A2: shown in blue) compared to the cloud-corrected at-sensor radiance (TOA: shown in red) (both shown in units of nW·cm^{-2}·sr^{-1}). Results are plotted along the full range of illumination conditions experienced by the DNB time series record (X-axis = Moon Illuminated Fraction %). For reference, the threshold (L_{min} = 3.0 nW·cm^{-2}·sr^{-1}) and breakthrough (L_{min} = 0.5 nW·cm^{-2}·sr^{-1}) performance specifications are shown as black-dotted and solid horizontal lines (respectively).

Table 2 Summary statistics for Benchmark Test #1; NTL (VZA, AOD). Values describe two key performance metrics for NASA's Black Marble product suite: (1) detection limit (L_{min}) and (2) robustness (L_0). Results are based on a discrete range of View Zenith Angles (VZA < 45°, VZA ≥45°) and Aerosol Optical Depths (AOD < 0.5, AOD ≥ 0.5) captured from all available (2012-YTD) cloud-corrected background NTL pixels for 30 VIIRS Level 3 tiles (10° x 10°).

TILE ID	Minimum Detectable Radiance (L_{min})				Retrieval Uncertainty @ L_{min} (L_0)			
	TOA	VNP46A2	TOA	VNP46A2	TOA	VNP46A2	TOA	VNP46A2
	Moon Fraction < 50%		Moon Fraction ≥ 50%		Moon Fraction < 50%		Moon Fraction ≥ 50%	
h10v05	0.558	0.370	1.829	0.255	0.052	0.050	1.040	0.021
h11v07	0.752	0.617	2.921	0.420	0.075	0.055	1.768	0.046
h12v09	0.331	0.203	2.411	0.140	0.076	0.019	1.687	0.012
h12v10	0.322	0.188	2.340	0.127	0.077	0.016	1.668	0.012
h12v11	0.400	0.289	2.384	0.156	0.062	0.036	1.601	0.032
h13v11	0.636	0.520	2.663	0.331	0.076	0.041	1.645	0.033
h17v08	0.400	0.252	2.910	0.154	0.095	0.031	2.009	0.020
h18v04	0.692	0.540	2.162	0.355	0.069	0.157	1.211	0.055
h18v05	0.563	0.336	3.968	0.210	0.136	0.075	2.869	0.013
h19v04	0.763	0.610	2.223	0.419	0.088	0.091	1.248	0.089
h20v11	0.336	0.221	2.475	0.124	0.065	0.022	1.734	0.023
h21v05	0.641	0.435	3.255	0.279	0.065	0.042	2.158	0.031
h22v05	0.714	0.535	3.398	0.319	0.077	0.032	2.229	0.043
h22v06	0.581	0.440	4.572	0.255	0.117	0.028	3.399	0.034
h23v05	0.543	0.350	2.844	0.208	0.073	0.040	1.964	0.027
h23v06	0.595	0.451	3.954	0.269	0.131	0.033	2.918	0.033
h24v05	0.446	0.226	2.963	0.129	0.070	0.039	2.132	0.024
h24v06	0.428	0.254	2.983	0.145	0.090	0.042	2.190	0.029
h25v05	0.517	0.296	3.023	0.169	0.045	0.047	2.055	0.018
h25v06	0.647	0.484	2.994	0.293	0.079	0.058	1.959	0.030
h25v07	0.641	0.521	2.715	0.317	0.076	0.048	1.725	0.032
h25v08	0.501	0.413	2.181	0.268	0.081	0.039	1.408	0.031
h26v05	0.425	0.206	3.142	0.110	0.092	0.040	2.335	0.019
h26v06	0.568	0.405	2.682	0.233	0.080	0.057	1.740	0.028
h26v07	0.428	0.326	2.051	0.188	0.067	0.041	1.325	0.026
h27v05	0.416	0.191	3.001	0.098	0.072	0.034	2.215	0.016
h27v06	0.410	0.241	2.494	0.122	0.066	0.037	1.733	0.023
h28v08	0.457	0.342	2.515	0.241	0.055	0.028	1.686	0.025
h29v05	0.580	0.359	2.379	0.204	0.058	0.053	1.444	0.022
h32v12	0.290	0.153	2.262	0.076	0.074	0.029	1.692	0.021

≤Goal Breakthrough ≥Threshold

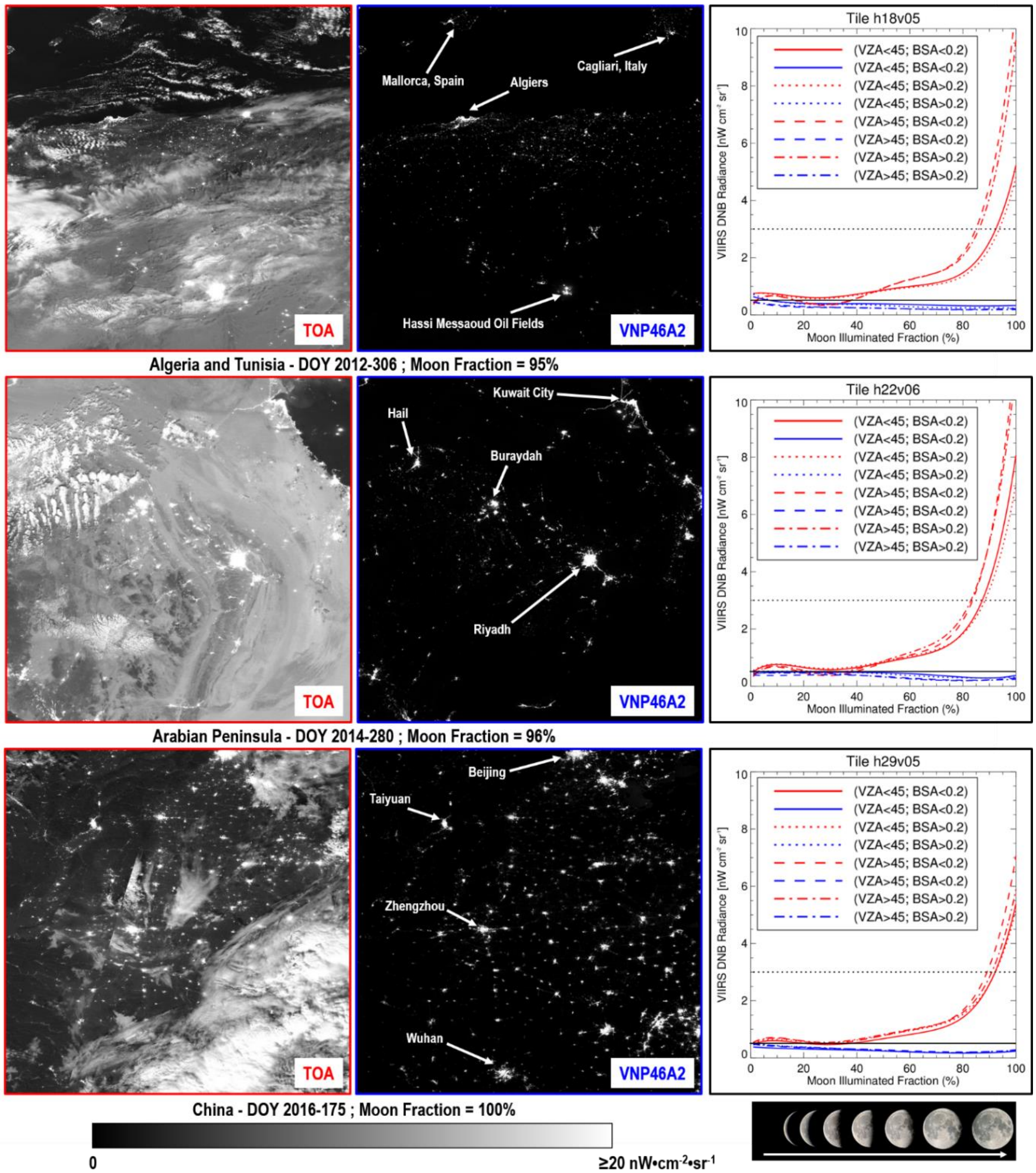

Figure 7 Benchmark Test #2: NTL (VZA, BSA). Note the dynamic range used for the Daily TOA and VNP46A2 scenes (Left and Center) is [0 to 20 nWatts·cm^{-2}·sr^{-1}]. Otherwise, setup is the same as **Figure 5**.

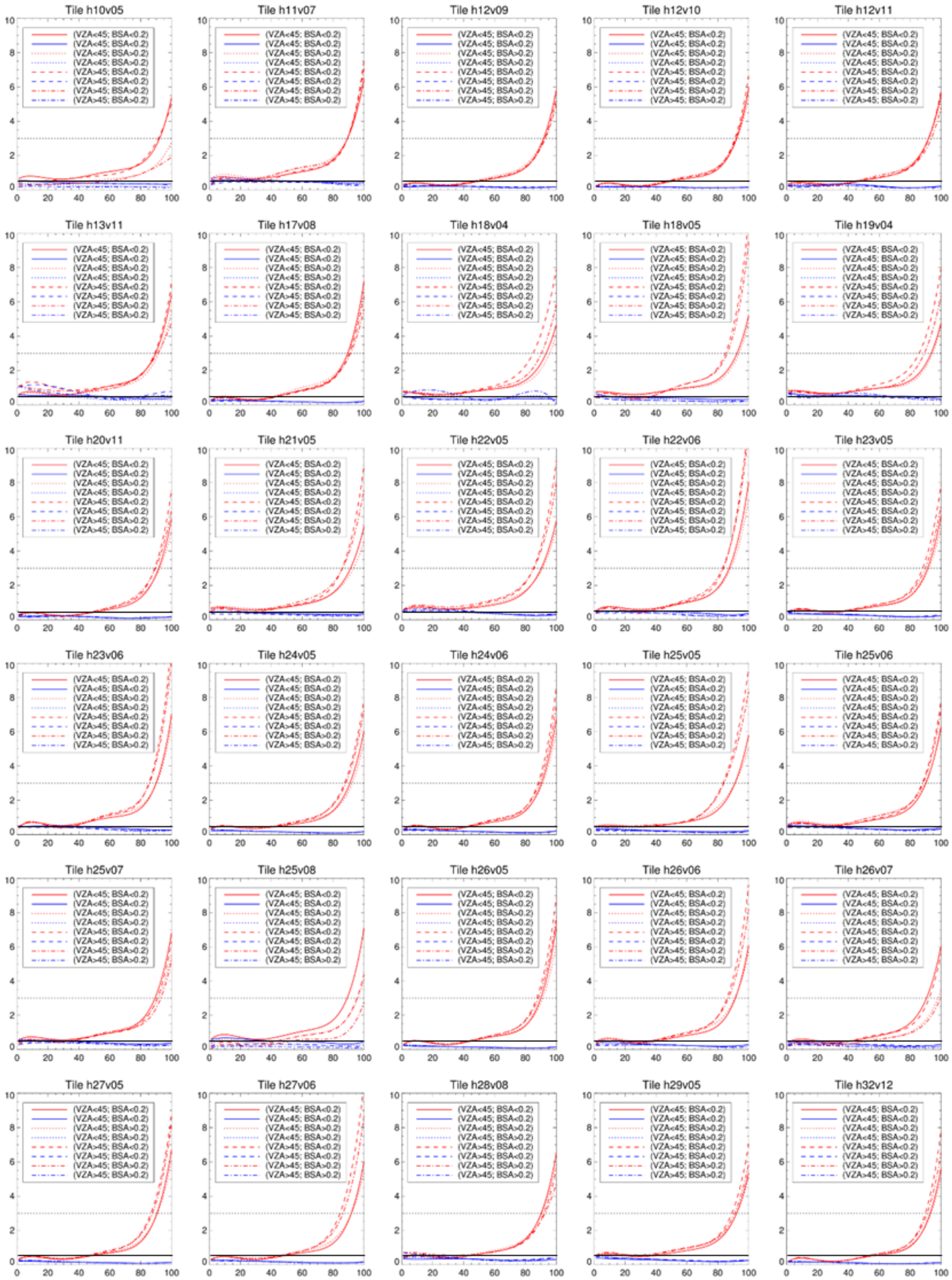

Figure 8 Results for Benchmark Test #2: NTL (VZA, BSA). Set up is the same as **Figure 6**.

Table 3 Summary statistics for Benchmark Test #2 – NTL (VZA, BSA) – based on a discrete range of View Zenith Angles (VZA < 45°, VZA ≥45°) and Black-Sky Albedos (BSA < 0.2, BSA ≥ 0.2). Set up is the same as **Table 2**.

TILE ID	Minimum Detectable Radiance (L_{min})				Retrieval Uncertainty @ L_{min} (L_0)			
	TOA	VNP46A2	TOA	VNP46A2	TOA	VNP46A2	TOA	VNP46A2
	Moon Fraction < 50%		Moon Fraction ≥ 50%		Moon Fraction < 50%		Moon Fraction ≥ 50%	
h10v05	0.645	0.406	2.373	0.326	0.089	0.045	1.360	0.029
h11v07	0.694	0.542	3.217	0.364	0.102	0.044	2.053	0.058
h12v09	0.378	0.243	2.520	0.154	0.085	0.033	1.747	0.015
h12v10	0.333	0.195	2.641	0.134	0.097	0.015	1.929	0.010
h12v11	0.391	0.267	2.538	0.164	0.085	0.027	1.761	0.034
h13v11	0.821	0.698	2.975	0.421	0.126	0.109	1.879	0.069
h17v08	0.419	0.267	2.948	0.160	0.100	0.032	2.010	0.018
h18v04	0.766	0.512	2.793	0.468	0.100	0.097	1.597	0.095
h18v05	0.661	0.417	3.512	0.278	0.116	0.084	2.394	0.014
h19v04	0.820	0.669	2.793	0.477	0.076	0.117	1.619	0.115
h20v11	0.356	0.232	2.958	0.135	0.085	0.019	2.196	0.018
h21v05	0.716	0.504	3.293	0.335	0.073	0.052	2.115	0.023
h22v05	0.720	0.531	3.326	0.321	0.068	0.025	2.198	0.049
h22v06	0.581	0.440	3.890	0.259	0.105	0.020	2.831	0.043
h23v05	0.545	0.339	2.963	0.200	0.076	0.028	2.071	0.031
h23v06	0.599	0.440	3.709	0.266	0.118	0.030	2.695	0.037
h24v05	0.462	0.236	2.983	0.137	0.068	0.036	2.143	0.024
h24v06	0.440	0.256	3.186	0.146	0.098	0.039	2.374	0.029
h25v05	0.542	0.307	3.231	0.188	0.065	0.040	2.237	0.019
h25v06	0.656	0.485	3.262	0.307	0.097	0.049	2.176	0.031
h25v07	0.697	0.552	3.166	0.337	0.089	0.054	2.038	0.032
h25v08	0.525	0.415	2.589	0.282	0.108	0.036	1.550	0.038
h26v05	0.442	0.215	3.222	0.118	0.095	0.041	2.415	0.022
h26v06	0.555	0.374	3.279	0.226	0.099	0.035	2.292	0.035
h26v07	0.573	0.437	2.786	0.272	0.098	0.052	1.793	0.030
h27v05	0.430	0.195	3.109	0.105	0.077	0.035	2.319	0.017
h27v06	0.429	0.242	3.290	0.125	0.076	0.037	2.428	0.020
h28v08	0.617	0.495	2.793	0.328	0.071	0.068	1.791	0.050
h29v05	0.617	0.370	2.746	0.221	0.070	0.063	1.749	0.021
h32v12	0.305	0.156	2.667	0.083	0.085	0.030	2.082	0.022

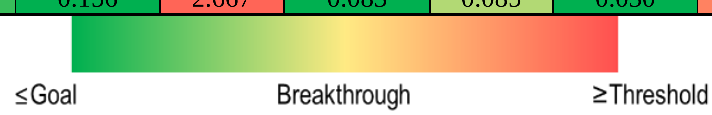

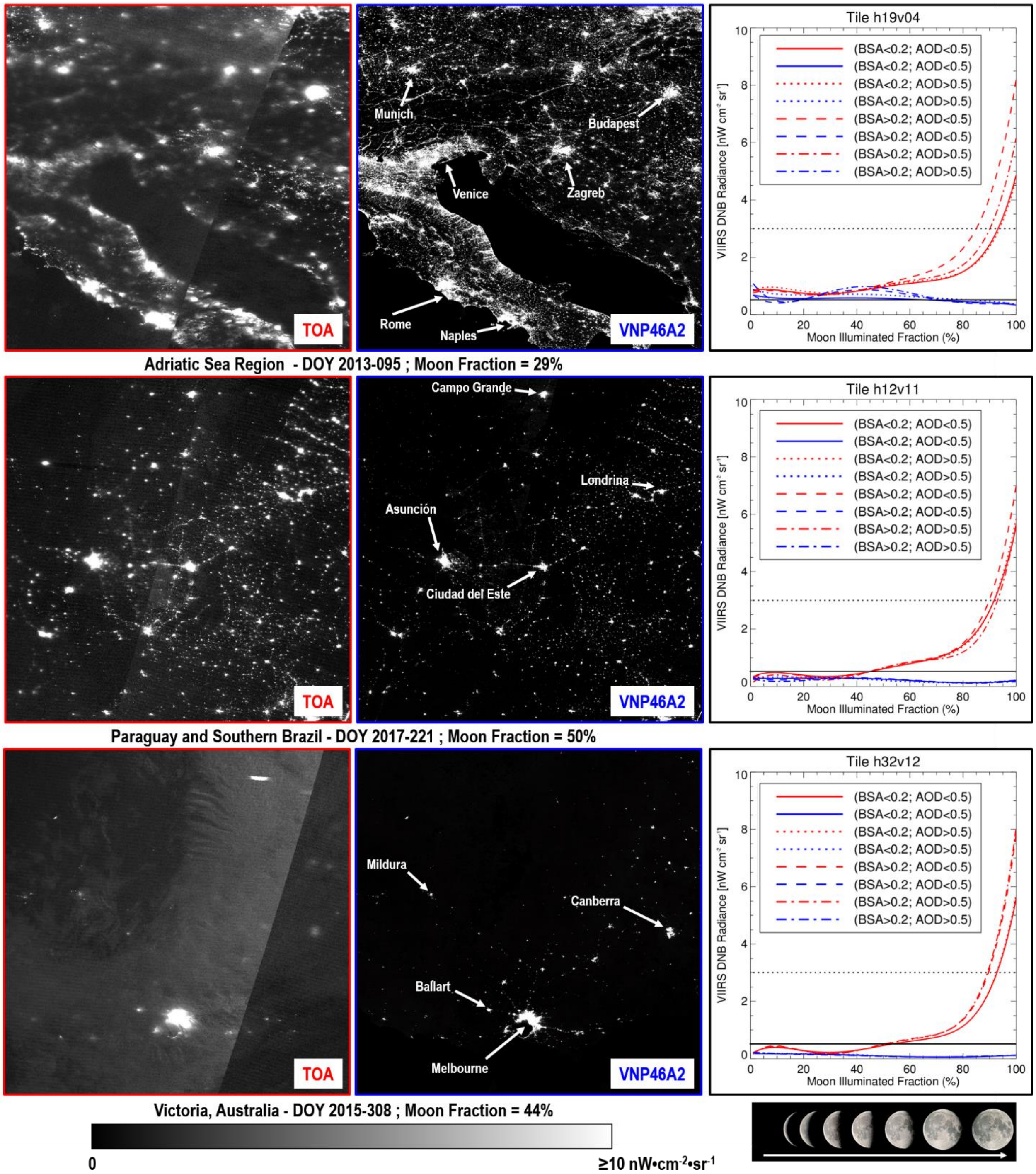

Figure 9 Benchmark Test #3: NTL (BSA, AOD). Note the Daily TOA and VNP46A2 scenes (Left and Center) exhibit half-moon to moonless conditions (Moon Fraction ≤ 50%). Otherwise, setup is the same as **Figure 6**.

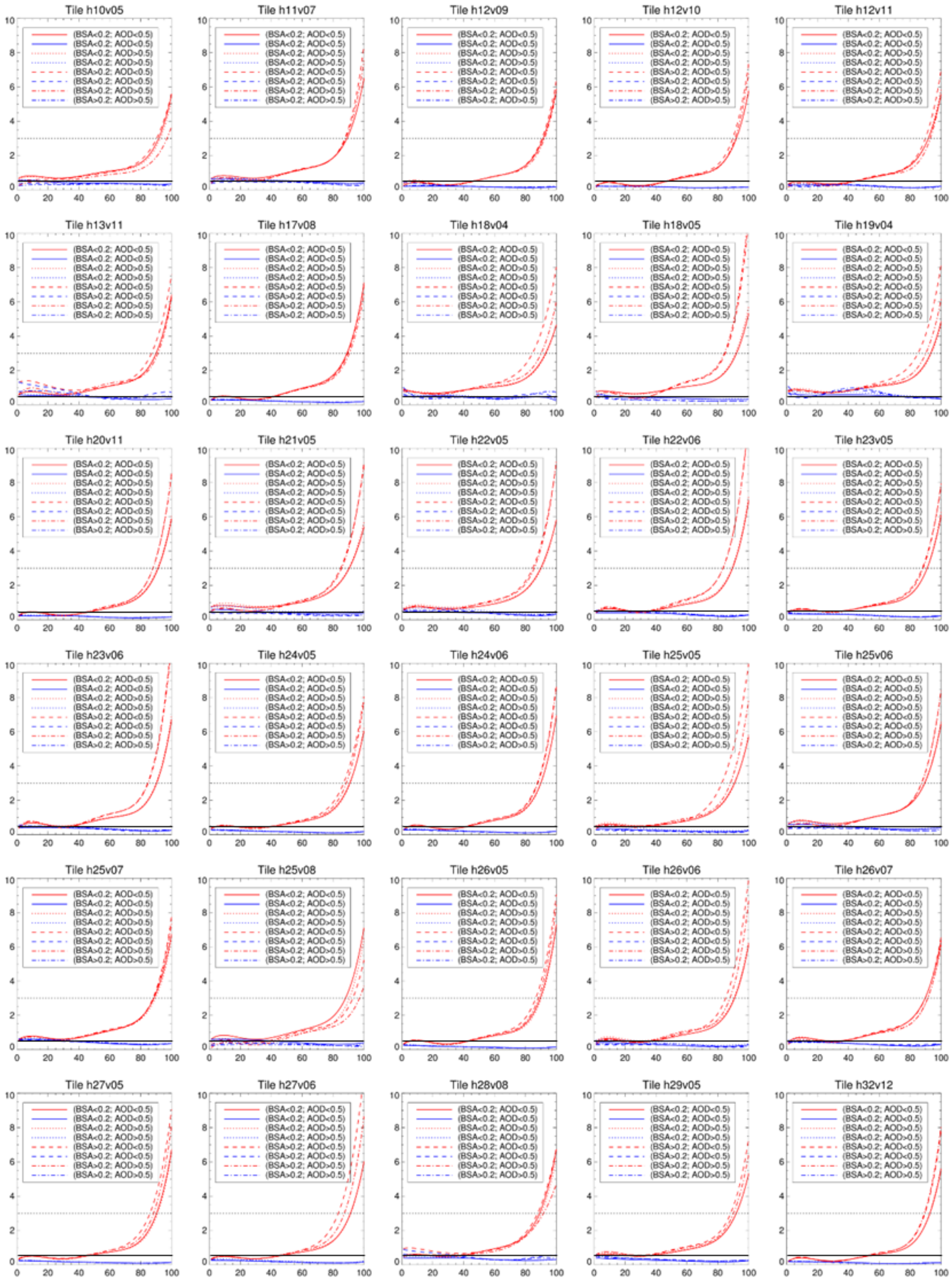

Figure 10 Results for Benchmark Test #3: NTL (BSA, AOD). Set up is the same as **Figure 6**.

Table 4 Summary statistics for Benchmark Test #3 – NTL (BSA, AOD) – based on a discrete range of Black-Sky Albedos (BSA < 0.2, BSA ≥ 0.2) and Aerosol Optical Depths (AOD < 0.5, AOD ≥ 0.5). Set up is the same as **Table 2**.

TILE ID	Minimum Detectable Radiance (L_{min})				Retrieval Uncertainty @ L_{min} (L_0)			
	TOA	VNP46A2	TOA	VNP46A2	TOA	VNP46A2	TOA	VNP46A2
	Moon Fraction < 50%		Moon Fraction ≥ 50%		Moon Fraction < 50%		Moon Fraction ≥ 50%	
h10v05	0.513	0.320	1.865	0.247	0.065	0.037	1.040	0.023
h11v07	0.684	0.532	3.059	0.387	0.114	0.048	1.934	0.058
h12v09	0.346	0.215	2.368	0.146	0.067	0.023	1.624	0.015
h12v10	0.313	0.175	2.480	0.127	0.085	0.012	1.791	0.009
h12v11	0.367	0.256	2.357	0.153	0.075	0.040	1.565	0.033
h13v11	0.819	0.691	2.753	0.415	0.107	0.117	1.694	0.078
h17v08	0.383	0.239	2.793	0.151	0.092	0.027	1.887	0.017
h18v04	0.678	0.484	2.646	0.382	0.082	0.116	1.590	0.091
h18v05	0.618	0.384	3.230	0.247	0.109	0.085	2.197	0.017
h19v04	0.738	0.549	2.715	0.393	0.076	0.080	1.661	0.075
h20v11	0.326	0.204	2.646	0.122	0.070	0.025	1.903	0.022
h21v05	0.638	0.422	3.009	0.276	0.064	0.048	1.942	0.023
h22v05	0.712	0.511	3.202	0.302	0.071	0.033	2.068	0.043
h22v06	0.618	0.451	3.997	0.286	0.099	0.023	2.879	0.039
h23v05	0.542	0.344	2.779	0.200	0.066	0.039	1.916	0.028
h23v06	0.604	0.454	3.593	0.281	0.121	0.029	2.575	0.045
h24v05	0.447	0.225	2.863	0.127	0.061	0.037	2.029	0.023
h24v06	0.431	0.255	2.986	0.146	0.090	0.041	2.197	0.029
h25v05	0.509	0.271	3.260	0.161	0.045	0.040	2.254	0.017
h25v06	0.631	0.466	3.065	0.291	0.083	0.057	2.014	0.024
h25v07	0.587	0.463	2.698	0.298	0.089	0.048	1.705	0.033
h25v08	0.467	0.372	2.047	0.252	0.091	0.044	1.281	0.036
h26v05	0.426	0.201	3.067	0.112	0.087	0.037	2.263	0.019
h26v06	0.519	0.337	3.150	0.204	0.091	0.040	2.181	0.033
h26v07	0.406	0.302	2.063	0.193	0.068	0.034	1.300	0.021
h27v05	0.419	0.187	3.073	0.099	0.070	0.033	2.282	0.016
h27v06	0.409	0.220	3.166	0.114	0.070	0.032	2.337	0.017
h28v08	0.531	0.409	2.537	0.284	0.064	0.054	1.673	0.044
h29v05	0.601	0.365	2.646	0.216	0.066	0.060	1.674	0.024
h32v12	0.289	0.143	2.484	0.076	0.080	0.028	1.916	0.021

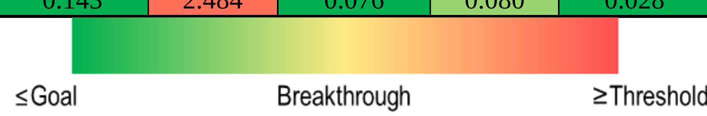

The individual (tile-based) benchmark test results in **Figure 6**, **Figure 8**, and **Figure 10** (which plot background NTL pixels as a function of moon-illuminated fraction) help illustrate how the refined product (VNP46A2) maintains a near constant background radiance profile across the entire lunar illumination cycle; well within the "Breakthrough" and the "Goal" performance requirements for L_{min} and L_0, respectively. In contrast, when using the cloud-corrected TOA product, only 27% of reported cases (all based on moonless periods, where Moon Fraction < 50%)

met the “Goal” requirement, while 37% of cases (all based on moonlit conditions, where Moon Fraction ≥ 50%) failed to meet the minimum “Threshold” requirement; indicating the TOA product’s lack of consistency (in a global sense), and its inaptness for applications requiring a stable NTL time series record for accurate characterization of change.

The albedo effect is shown to significantly influence NTL product performance, particularly during moonlit periods (Moon Fraction ≥ 50%). For most tiles, L_{min} values for TOA data with albedos less than 0.2 were consistently lower than values with BSA data higher than 0.2. For TOA products during moonlit periods, the influence of albedo was also more pronounced compared to AOD. Both the detection limit (L_{min}) and robustness (L_0) were also found to be larger (and therefore worse) over desert regions, e.g. the Saharan Desert (h18v05), the Middle East (h21v05, h22v05, h22v06, and h23v06), and the Tibetan Plateau (h26v05, h26v06, h27v05, and h27v06). For these cases, L_{min} and L_0 often failed to meet their “Threshold” performance requirements. While the increased level of measurement error in the TOA data can be anticipated for bright surface conditions, the fact that equally higher degradations for L_0 were observed suggests that additional higher-order effects (*e.g.,* increased influence of anisotropic diffuse illumination and multiple scattering) are also impacting NLT retrieval quality. This was especially true for desert areas, where the total uncertainty of the product (L_{min} + L_0) is shown to be higher than the L_{min} “Threshold” performance requirement by a factor of at 1.6x to 2.0x.

We also found that the restricted use of TOA data under moonless nights does not necessarily result in a higher-quality NTL retrieval; even for conditions experiencing lower AOD and albedos (**Figure 6** and **Figure 8**). In fact, 98.3% of VNP46A2 benchmark test results under moonlit conditions, for both L_{min} and L_0, were actually lower (and thus better) than the TOA benchmark test results under moonless conditions (**Table 2**, **Table 3**, and **Table 4***)*. These benchmark tests, therefore, help confirm the temporal consistency of the VNP46A2 product across the entire moon-illuminated cycle.

4.1.2. Performance of the VIIRS Nighttime Cloud Mask

Another key factor that affects the quality of NTL products is the performance of the VIIRS Nighttime Cloud Mask (VCM). Accordingly, we conducted the following benchmark test to establish the following question:

- **Benchmark Test #4:** What is the fraction of confidently clear land-based nighttime VCM detections that were flagged by the VNP46 algorithm as less than a high-quality NTL retrieval?

The goal of this test is to establish the overall skill of the VCM to correctly map confidently clear nighttime pixels, which (in the absence of additional post-processing steps) can lead to a high-quality NTL retrieval. The performance metric is expressed in terms of the probability of correct typing (PCT) (Kopp et al., 2014). We established PCT values by counting the total number of confidently clear VCM pixels that were subsequently flagged for additional inspection. Flagging of suspect VCM detections is done in the Lunar BRDF correction process (nighttime branch), which outputs a poor-quality mandatory QA flag when the VNP46 algorithm fails to produce a reliable NTL result, and through additional consistency checks conducted during the temporal gap-filling process.

Results for benchmark tests #4 (**Table 5** and **Table 6**) illustrate how the performance of the nighttime VCM varies significantly depending on factors such as moon-illumination conditions, surface albedo (*e.g.*, retrieval conditions with high albedos, *e.g.*, desert and snow have worst PCT values), as well as atmospheric, climatic, and geographic conditions. The VCM performance requirement established by the JPSS program is ≥ 88% PCT. This requirement only applies to thick clouds optical thickness (COT) greater than 1.0 tau. This is a challenge for NTL time series detection, particularly since thin cirrus and low cloud fields often lead the VCM to think that the NTL pixel is clear. In addition to NTL attenuation caused by clouds with COT values less than 1.0 tau, the scattering effects in terms of light diffusion and even side-illumination can introduce spurious results.

Results point to a PCT of 89.03% under moonless conditions, 81.92% under moonlit conditions, and a global PCT of 85.5% under all conditions tested. Note that the PCT values reported in this test only describe the overall performance of the VCM vis-à-vis the NASA Black Marble NTL data processing chain. As such, results are not representative of the true performance characteristics of the nighttime VCM product.

Table 5 Summary statistics for Benchmark Test #4 (VCM Performance Test). Values describe the total probability of correct typing (PCT) corresponding to each sample VIIRS Level 3 tile, as well as for six different groupings (as done in benchmark tests #1 to #3) based on a discrete range of BSA, VZA, and AOD values observed for moon illuminated fractions < 50%.

TILE ID	Total PCT	PCT By Grouping (Moon Fraction < 50%)					
		VZA < 45°	VZA ≥ 45°	BSA < 0.2	BSA ≥ 0.2	AOD < 0.5	AOD ≥ 0.5
h10v05	90.46%	91.30%	89.01%	94.27%	67.27%	90.85%	88.65%
h11v07	92.66%	94.22%	91.00%	95.69%	69.37%	92.98%	91.82%
h12v09	92.62%	95.72%	89.37%	94.64%	74.81%	93.14%	91.02%
h12v10	92.96%	94.19%	91.59%	96.07%	71.10%	92.95%	92.99%
h12v11	91.62%	91.83%	91.35%	96.89%	62.01%	91.59%	91.81%
h13v11	93.62%	93.48%	93.78%	97.17%	70.21%	93.88%	92.32%
h17v08	93.15%	95.29%	90.92%	95.57%	72.54%	94.42%	91.30%
h18v04	82.26%	88.05%	69.71%	85.31%	71.55%	83.58%	72.15%
h18v05	87.17%	87.13%	87.25%	87.92%	87.02%	87.44%	86.67%
h19v04	80.86%	88.28%	66.12%	82.93%	72.94%	82.79%	68.63%
h20v11	79.90%	88.50%	70.65%	82.86%	71.53%	79.04%	83.19%
h21v05	83.64%	85.39%	81.26%	88.56%	80.00%	84.67%	81.15%
h22v05	86.43%	86.89%	85.69%	92.07%	83.33%	87.06%	85.16%
h22v06	86.91%	86.87%	86.96%	80.91%	87.54%	86.62%	87.38%
h23v05	85.63%	86.20%	84.72%	91.16%	82.21%	86.34%	84.18%
h23v06	85.70%	86.33%	84.91%	85.82%	85.67%	85.74%	85.63%
h24v05	86.00%	86.62%	84.99%	90.53%	83.73%	86.63%	84.53%
h24v06	85.85%	86.41%	85.10%	90.23%	82.00%	85.91%	85.76%
h25v05	89.09%	89.46%	88.51%	92.04%	86.06%	89.28%	88.46%
h25v06	90.55%	90.82%	90.21%	96.78%	78.38%	90.65%	90.42%
h25v07	92.54%	93.38%	91.62%	96.76%	66.31%	92.91%	91.93%
h25v08	94.65%	95.78%	93.47%	96.99%	77.40%	95.50%	92.59%
h26v05	89.36%	89.93%	88.45%	88.66%	89.63%	89.39%	89.26%
h26v06	91.08%	91.21%	90.91%	95.80%	70.67%	91.59%	90.32%
h26v07	91.67%	92.50%	90.73%	95.53%	62.05%	92.75%	89.97%
h27v05	90.26%	90.65%	89.65%	92.76%	88.23%	90.54%	89.25%
h27v06	92.84%	93.75%	91.69%	95.43%	77.05%	93.51%	90.60%
h28v08	94.48%	97.20%	91.72%	95.85%	83.87%	95.24%	91.62%
h29v05	89.69%	90.76%	88.01%	94.56%	66.68%	90.30%	88.30%
h32v12	87.32%	86.92%	87.97%	93.90%	57.94%	87.36%	87.06%

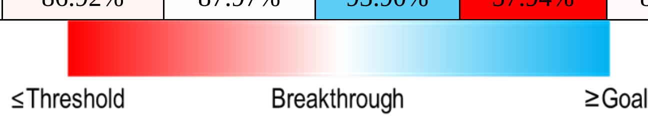

Table 6 Summary statistics for Benchmark Test #4 (VCM Performance Test) describe the total probability of correct typing (PCT) under moon illuminated fractions ≥ 50%. Setup is the same as **Table 5**.

TILE ID	Total PCT	PCT By Grouping (Moon Fraction ≥ 50%)					
		VZA < 45°	VZA ≥ 45°	BSA < 0.2	BSA ≥ 0.2	AOD < 0.5	AOD ≥ 0.5
h10v05	84.77%	86.50%	81.79%	87.26%	68.86%	85.09%	83.23%
h11v07	82.06%	83.75%	80.23%	83.52%	71.17%	82.91%	79.84%
h12v09	86.83%	88.74%	84.90%	88.23%	72.55%	87.65%	84.49%
h12v10	85.99%	86.36%	85.59%	87.14%	77.57%	86.27%	84.94%
h12v11	88.76%	88.93%	88.55%	91.03%	74.63%	89.15%	86.66%
h13v11	88.17%	87.89%	88.53%	89.93%	74.51%	88.56%	86.38%
h17v08	87.70%	89.51%	85.85%	88.92%	76.23%	90.60%	83.55%
h18v04	79.38%	85.41%	66.37%	79.63%	78.58%	80.40%	70.96%
h18v05	75.68%	76.27%	74.78%	76.70%	75.50%	76.38%	74.37%
h19v04	77.97%	85.35%	62.87%	78.46%	76.18%	79.84%	65.17%
h20v11	74.69%	83.05%	65.54%	72.00%	82.14%	74.16%	76.62%
h21v05	76.44%	79.30%	72.56%	76.98%	76.10%	77.28%	74.32%
h22v05	78.79%	79.66%	77.37%	81.41%	77.69%	79.55%	77.19%
h22v06	71.92%	72.46%	71.24%	69.30%	72.16%	72.65%	70.73%
h23v05	79.71%	80.16%	78.99%	78.86%	80.09%	79.81%	79.49%
h23v06	71.90%	72.57%	71.08%	73.19%	71.56%	71.68%	72.32%
h24v05	80.22%	80.99%	78.94%	78.09%	80.97%	80.16%	80.37%
h24v06	77.88%	78.63%	76.88%	76.30%	78.96%	77.77%	78.04%
h25v05	82.40%	83.31%	80.91%	83.63%	81.34%	82.07%	83.55%
h25v06	81.95%	83.19%	80.39%	82.41%	81.22%	82.81%	80.86%
h25v07	83.58%	85.01%	82.02%	84.82%	76.21%	85.63%	80.36%
h25v08	86.40%	88.96%	83.76%	86.91%	82.59%	88.31%	82.39%
h26v05	82.11%	82.98%	80.75%	79.72%	82.76%	81.93%	82.96%
h26v06	82.74%	84.03%	81.12%	83.94%	77.77%	84.43%	80.14%
h26v07	84.30%	85.50%	82.96%	85.50%	73.18%	87.66%	79.46%
h27v05	82.47%	83.00%	81.61%	84.16%	81.41%	82.58%	82.04%
h27v06	85.45%	86.27%	84.42%	86.29%	79.72%	86.34%	82.45%
h28v08	90.59%	92.61%	88.55%	90.96%	87.12%	92.15%	84.73%
h29v05	83.75%	85.80%	80.51%	85.02%	78.30%	85.17%	80.24%
h32v12	82.89%	83.38%	82.09%	83.95%	79.19%	83.82%	76.30%

This is particularly the case since NTL artifacts (*e.g.,* Aurora and mid- to- high latitudes), while temporary in nature, can also set off the product's QA flags; thus, resulting in slightly lower VCM PCT values. Nevertheless, these benchmark test provide insight into potential areas for improvement in the VCM algorithm. In particular, the comparatively lower PCT values under moonlit conditions underscore the need for considering variations in surface brightness, as routinely done in daytime VCM processing.

4.1.3. Pixel-Based Variations in NTL

The increased utility of the VIIRS Day/Night Band sensor to capture sub-pixel NTL features, has led to a considerable number of studies that have utilized the underlying radiances directly at the pixel-level (Cao and Bai, 2014; Chen et al., 2015; Elvidge et al., 2015a; Guo et al., 2015; Hu et al., 2015; Lee et al., 2014; Mann et al., 2016; Ou et al., 2015; Sharma et al., 2016; Shi et al., 2014; Straka et al., 2015; Zhao et al., 2016). The wide range of applications makes it therefore necessary to establish the sensitivity of residual errors and extraneous artifacts in the NTL retrievals through explicit assessment of product performance at the native pixel scale. Accordingly, we conducted a series of pixel-based benchmark tests to address the following three questions:

– **Benchmark Test #5:** What is the fraction of the variation in the pixel-based NTL time series that can be explained by variations in moon-illuminated reflectance anisotropy (hereby termed the lunar BRDF effect)?

– **Benchmark Test #6:** What is the fraction of the variation in the pixel-based NTL time series that can be explained by changes in snow cover?

– **Benchmark Test #7:** What is the fraction of the variation in the pixel-based NTL time series that is explained by seasonal changes in canopy-level foliage?

The performance metrics for benchmark tests #5 and #6 are both expressed in terms of the square of Pearson coefficient (R2 x 100%) between the 5-year NTL daily time series data and the periodicity of the lunar cycle (defined using daily values of moon-illumination fraction). To estimate the R2, we fitted a 5th order polynomial between these two variables - i.e., NTL(Moon Illuminated Fraction) – to establish the same relationships observed in **Figure 5-Figure 10** at the individual pixel-level.

For these three tests, we employed a random stratified sample of 72,000 individual TOA and VNP46A2 grid cells representing a diverse range of urban covers, surface conditions, and latitudinal gradients. As with benchmark tests #1 to #3, these tests were based on the entire available Collection V001 DNB time series record (2012-mid 2017), comprising the same sample Level-3 tiles listed in **Table 2-Table 4**.

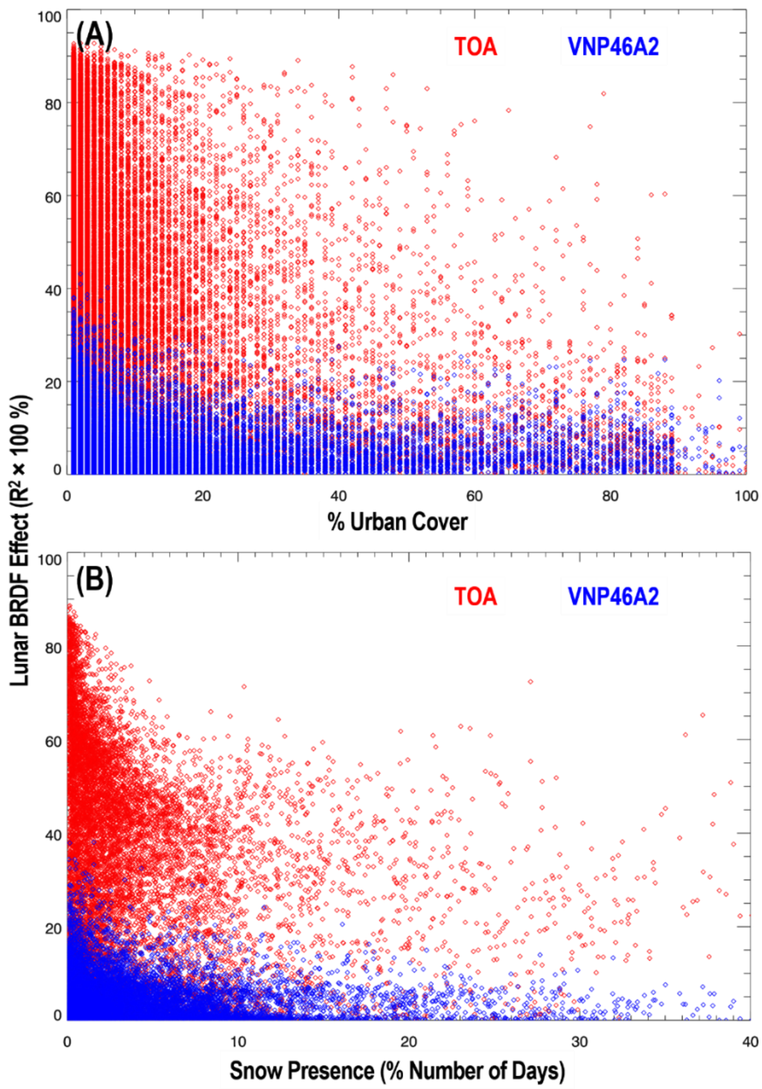

Figure 11 The correlation between a 5-year time series of daily nighttime lights (NTL) and lunar phase for the cloud-corrected at-sensor DNB radiance product (TOA: shown in red) and NASA's Black Marble daily moonlight adjusted nighttime lights (NTL) product (VNP46A2: shown in blue) shown as a function of (A) percent urban cover (benchmark test #5) and (B) snow presence (benchmark test #6).

In order to establish realistic NTL detection limits relative to anticipated changes in NTL, we used the Global Urban Footprint product (Esch et al., 2017, 2013) to ensure that the stratified sample was also spatially representative of different stages of urban growth – from sparse rural (% Urban = 0) to densely built-up pixels (% Urban = 100%). Results for benchmark test #5 are illustrated in **Figure 11(A)**. Note that, in the case of the TOA product, benchmark test #5 measures the degree of dependence in L_{DNB} (*cf.*, Equation 1) to Lunar BRDF effects (after cloud correction) for a wide range of percent urban covers.

Conversely, for the refined product (VNP46A2), this test measures the residual variance in L_{NTL} caused by lunar reflectance anisotropy effects after cloud-, atmospheric-, BRDF-, and seasonal (P_{gap}) correction. Results for the VNP46A2 product, therefore, demonstrate how the lunar BRDF effect can be reduced down to a Pearson R^2 coefficient of 0.37, across low-density urban pixels (and thus, low-intensity NTL), and even lower (< 0.10) for high density urban pixels (and thus, high-intensity NTL). The VNP46A2 product enhancements, therefore, result in a substantial reduction of residual lunar contamination relative to the cloud-cleared TOA data, which had high R^2 values, ranging from [0.4, 0.9], for DNB pixels experiencing both low to high percent urban covers.

Results for benchmark test #6 illustrate the TOA and VNP46A2 products' performance as a function of observed variations in snow cover (**Figure 11B**). The dependence of the pixel-based values to Lunar BRDF effects, resulting from moon-reflected snow surfaces, remained well < 0.30 (Pearson R^2 coefficient), a substantial enhancement relative to the cloud-cleared TOA data. Since the Lunar BRDF effect was measured as a function of the number of cloud-free snow-covered days within each DNB grid cell, benchmark test #6 can be used to assess the ability of the NASA Black Marble algorithm to effectively capture snow-covered surfaces. The comparatively lower R^2 values across VNP46A2 pixels with short snow days (< 10% of the S-NPP time series) demonstrate the VNP46A2 product's ability to correctly activate the current day snow status flag – a critical step for triggering the snow BRDF/albedo algorithm process necessary to mitigate downstream errors in the VNP46 product. This is particularly relevant for NTL conditions experiencing short but intense periods of snow cover; where highly reflective snow can introduce large positive biases in the final NTL estimates (Bennett and Smith, 2017; Levin, 2017; Román and Stokes, 2015). It is also necessary for robust outlier detection; where the actual moon/aerosol/albedo contribution is needed to establish the boundary NTL conditions.

This latter idea is demonstrated in **Figure 4**, where extraneous light emissions caused by the Aurora Borealis north of Lake Superior were located over snow- and cloud-contaminated DNB pixels. This would have led to significant errors of cloud-, snow-, and aurora-leakage, which, due to the use of BRDF corrected pixels as a baseline, were correctly classified as outliers by the VNP46 algorithm. Such higher order effects, which are common at daily time scales, underscore the need to routinely retrieve daily DNB BRDF quantities to better account for these rapidly changing scenarios. We found that a standalone climatology, based on a-priori (annual or monthly) DNB BRDF values, while useful for helping mitigate data gaps in the daily BRDF time series, resulted in increased contamination from ephemeral snow and other changing conditions.

Results for benchmark test #7 illustrate how the seasonal increase in canopy-level foliage during the winter and summer months (as described in Section 2.1.3) does not affect the trend in the VNP46A2 NTL time series record. This refinement is illustrated in the sample plots shown in **Figure 12**, where the pixel-level VNP46A2 values (blue points) do not predominate along the central region of the 2nd quadrant ($X \leq 0$; $Y \geq 0$, or the area inside the dotted black circles in **Figure 12**), where increases in the magnitude of NTL during winter periods track corresponding increases in green foliage between summer and winter periods. The seasonal effect was found to be most pronounced across temperate regions (*e.g.,* US, European, and Asia tiles: h10v05; h18v04; h18v05; h24v05; h25v05; h26v05; h29v05) as confirmed by previous studies (Bennett and Smith, 2017; Levin, 2017; Levin and Zhang, 2017). We also found additional seasonal variations across sample Level 3 tiles in West Africa (h17v08) and South Africa (h20v11); suggesting that seasonal variations in NTL are likely to be more pervasive than originally thought. Previous assessments had thus far examined the seasonal variations using spatially- and temporally-aggregated NTL products (*e.g.,* monthly moon-free composites at city-wide scales). The results from benchmark test #7, however, provide additional new insights of the variations at finer spatial and temporal scales.

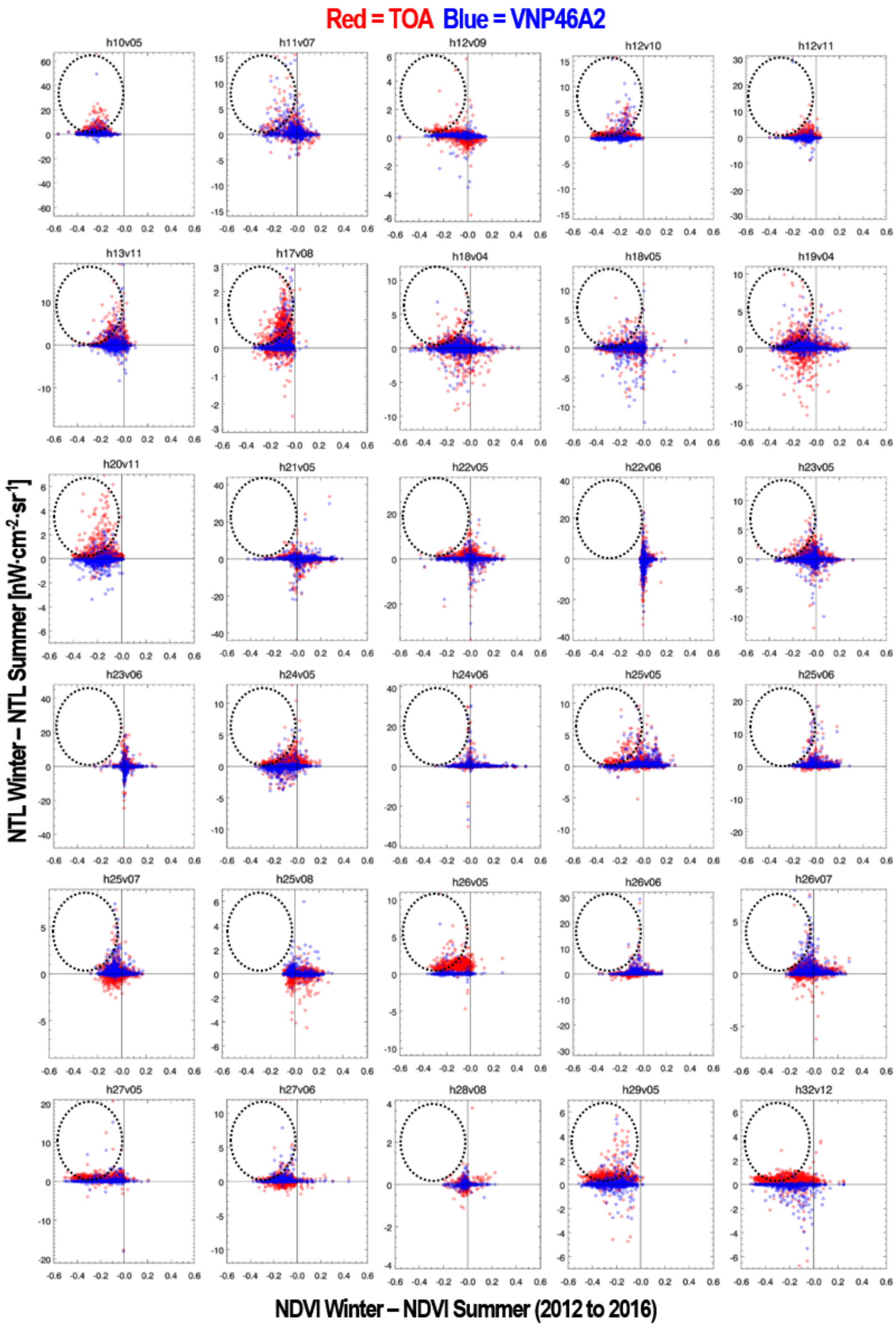

Figure 12 Results for benchmark test #7. The effects of seasonal variations of NTL with NDVI between winter and summer periods (i.e., pixels within black-dotted circles in upper-left quadrants) are shown for 30 sample Level 3 tiles for the cloud-corrected at-sensor DNB radiance product (TOA: shown in red), and NASA's Black Marble daily moonlight adjusted nighttime lights (NTL) product (VNP46A2: shown in blue).

4.2. Validation Approach

The series of benchmark tests introduced in Section 4.1 were designed to quantify errors inherited from the upstream products (i.e., VIIRS calibrated radiances, cloud mask, aerosol retrieval, etc.) These evaluations, however, only provide a relative assessment of NTL product performance. To establish the absolute accuracy of the final NTL retrievals, one must also assess the NTL products against an independent source of reference data. Unfortunately, quality-assessed in-situ NTL measurements are not widely available; let alone, at the spatial and temporal densities necessary to capture the full range of retrieval conditions. Recent NASA Black Marble product validation efforts have therefore focused on developing guidelines for accuracy assessment of NTL products through a number of international initiatives described in the following subsections.

4.2.1. GEO's Nighttime Product Validation Task

Under the Group on Earth Observations (GEO) Human Planet Initiative's 2017-2019 Work Programme, a Nighttime Product Validation (NPV) task was recently established to foster the development of advanced accuracy assessment of NTL time series products. A key deliverable of the NPV task is the development of a good practices protocol focusing on quantitative validation of satellite-derived NTL products. Key components to be included as part of this protocol, are: (1) variable definitions and accuracy metrics following traceable units of the Système Internationale (SI); (2) best practice guidelines for field sampling and scaling techniques; (3) recommendations for reporting and use of accurate information; (4) guidelines for product inter-comparison exercises; and (5) recommendations for data and information exchange.

4.2.2. Pitahaya Field Experiment

Under technical guidance from GEO Human Planet Initiative's NPV task, Puerto Rico's Working Group on Light Pollution (PRWGLP) seeks to develop measurement standards and protocols for in-situ data collection. The primary driver for this activity is the development of a sustainable development indicator, based on NTL time series data, to better meet the multiple regulatory and scientific aspects of PR's light pollution laws and ordinances. To that end, a number of scoping exercises were recently conducted across multiple light pollution abatement zones in Puerto Rico. This included a successful deployment of a stable point source of light at the Pitahaya Farmland site in Cabo Rojo, PR (**Figure 13**).

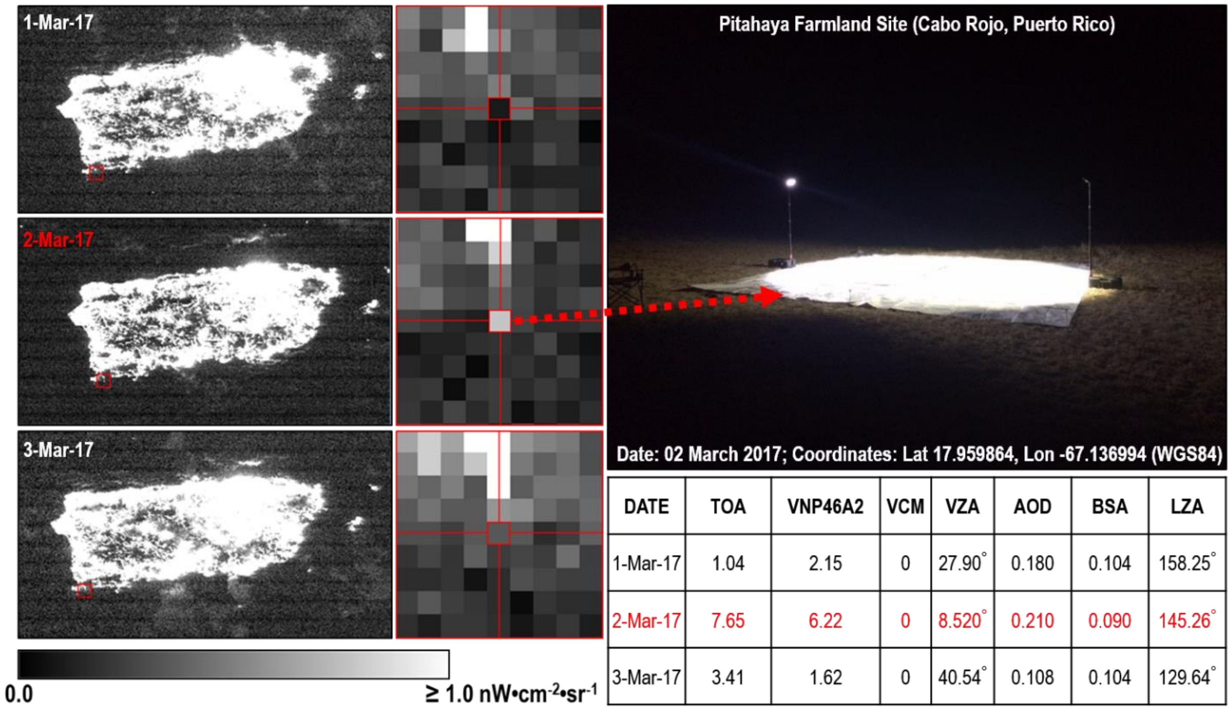

DATE	TOA	VNP46A2	VCM	VZA	AOD	BSA	LZA
1-Mar-17	1.04	2.15	0	27.90°	0.180	0.104	158.25°
2-Mar-17	7.65	6.22	0	8.520°	0.210	0.090	145.26°
3-Mar-17	3.41	1.62	0	40.54°	0.108	0.104	129.64°

Figure 13 The NTL radiances at the Pitahaya Farmland site in Cabo Rojo, PR on 1st, 2nd and 3rd March, 2017. The Top-Right image shows the setup of the stable point source. TOA and VNP46A2 values are in nW·cm-^{2}·sr-^{1}. VCM = 0 represents cloud free overpasses. LZA is lunar zenith angle, and the values larger than 108° correspond to moonless nights.

During the night of 2 March, 2017, at 2:00 local time, the PRWGLP team conducted a validation experiment at the aforementioned Pitahaya site. A stable point source was reflected by a 30 m^2 Lambertian target to generate an in-band DNB radiance at sensor (L_{DNB}) of ~0.45nW·cm^{-2}·sr^{-1}. Additional Sky-Quality Meter (SQM) data recordings (Falchi et al., 2016; Kyba et al., 2013, 2011; Schnitt et al., 2013) with specialized filters matching the VIIRS relative spectral response (RSR), as well as atmospheric measurements from nearby AERONET sun photometers (Holben et al., 1998) were used to characterize atmospheric conditions.

The validation approach follows the assessment method first described in *Cao and Bai* (2014), which relies on quantitative analysis and stability monitoring of stable light point sources. We used the following parameters to generate our radiative transfer calculations: (1) atmospheric transmittance=0.80 (based on 6S radiative transfer code and AERONET calculations), a target reflectance = 0.8, and 16W of total effective irradiance incident on the reflective surface. Results in **Figure 13** also illustrate how the detected VIIRS at-sensor cloud-corrected radiance (TOA) and

VNP46A2 estimates over the pixel centered on the reflective point source were within the VNP46A2 product's "Breakthrough" requirement for L_{min} (0.43 $nW \cdot cm^{-2} \cdot sr^{-1}$) – after removing background noise measured the days prior and after activation of the stable light point sources. We found that the final VNP46A2 product resulted in a 16.95% sensitivity enhancement (due to improved reduction background noise), as confirmed in previous benchmark tests, compared to the at-sensor cloud-corrected radiance product (TOA) under observed moon-free conditions.

5. DATA FORMAT

5.1. Format

NASA's Black Marble data are provided in the standard land HDF-EOS (Hierarchical Data Format - Earth Observing System) format. The filenames follow a naming convention which gives useful information regarding the specific product. For example, the filename VNP46A1.A2015001.h08v05.001.2017012234657.h5 indicates:

- VNP46A1- Product Short Name
- . A2015001- Julian Date of Acquisition (A-YYYYDDD)
- .h08v05 - Tile Identifier (horizontalXXverticalYY)
- .001 - Collection Version
- . 2017012234657- Julian Date of Production (YYYYDDDHHMMSS)
- .h5 - Data Format HDF5

Table 7 Scientific Data Sets included in the VNP46A1 Product

Scientific Datasets (SDS HDF Layers)	Units	Description	Bit Types	Fill Value	Valid Range	Scale Factor	Offset
DNB_At_Sensor_Radiance	$nW \cdot cm^{-2} \cdot sr^{-1}$	At-sensor DNB radiance	16-bit unsigned integer	65535[1]	0 - 65534	0.1	0.0
Sensor_Zenith	Degrees	Sensor zenith angle	16-bit signed integer	-32768	-9000 - 9000	0.01	0.0
Sensor_Azimuth	Degrees	Sensor azimuth angle	16-bit signed integer	-32768	-18000 – 18000	0.01	0.0
Solar_Zenith	Degrees	Solar zenith angle	16-bit signed integer	-32768	0 – 18000	0.01	0.0
Solar_azimuth	Degrees	Solar azimuth angle	16-bit signed integer	-32768	-18000 – 18000	0.01	0.0
Lunar_Zenith	Degrees	Lunar zenith angle	16-bit signed integer	-32768	0 – 18000	0.01	0.0
Lunar_Azimuth	Degrees	Lunar azimuth angle	16-bit signed integer	-32768	-18000 – 18000	0.01	0.0
Glint_Angle	Degrees	Moon glint angle	16-bit signed integer	-32768	-18000 – 18000	0.01	0.0
UTC_Time	Decimal hours	UTC time	32-bit floating point	-999.9	0 24	1.0	0.0
QF_Cloud_Mask[2]	Unitless	Cloud mask status	16-bit unsigned integer	65535	0 - 65534	N/A	N/A
QF_DNB[3]	Unitless	DNB quality flag	16-bit unsigned integer	65535	0 - 65534	N/A	N/A
Radiance_M10	$W \cdot m^{-2} \cdot \mu m^{-1} \cdot sr^{-1}$	Radiance in band M10	16-bit unsigned integer	65535	0 - 65534	0.0013	-0.04
Radiance_M11	$W \cdot m^{-2} \cdot \mu m^{-1} \cdot sr^{-1}$	Radiance in band M11	16-bit unsigned integer	65535	0 - 65534	0.00058	-0.02
BrightnessTemperature_M12	Kelvins	Brightness temperature of band M12	16-bit unsigned integer	65535	0 - 65534	0.0025	203.0

BrightnessTemperature_M13	Kelvins	Brightness temperature of band M13	16-bit unsigned integer	65535	0 - 65534	0.0025	203.0
BrightnessTemperature_M15	Kelvins	Brightness temperature of band M15	16-bit unsigned integer	65535	0 - 65534	0.0041	111.0
BrightnessTemperature_M16	Kelvins	Brightness temperature of band M16	16-bit unsigned integer	65535	0 - 65534	0.0043	103.0
QF_VIIRS_M10[4]	Unitless	Quality flag of band M10	16-bit unsigned integer	65535	0 - 65534	N/A	N/A
QF_VIIRS_M11[4]	Unitless	Quality flag of band M11	16-bit unsigned integer	65535	0 - 65534	N/A	N/A
QF_VIIRS_M12[4]	Unitless	Quality flag of band M12	16-bit unsigned integer	65535	0 - 65534	N/A	N/A
QF_VIIRS_M13[4]	Unitless	Quality flag of band M13	16-bit unsigned integer	65535	0 - 65534	N/A	N/A
QF_VIIRS_M15[4]	Unitless	Quality flag of band M15	16-bit unsigned integer	65535	0 - 65534	N/A	N/A
QF_VIIRS_M16[4]	Unitless	Quality flag of band M16	16-bit unsigned integer	65535	0 - 65534	N/A	N/A
Moon_Phase_Angle	Degrees	Moon phase angle	16-bit signed integer	-32768	0 – 18000	0.01	0.0
Moon_Illumination_Fraction	Percentage	Moon illumination fraction	16-bit signed integer	-32768	0 – 10000	0.01	0.0
Granule	Unitless	Number of selected Granule	8-bit unsigned integer	255	0 - 254	1.0	0.0

Table 8 Scientific Data Sets included in the VNP46A2 Product

Scientific Data Sets (SDS HDF Layers)	**Units**	**Description**	**Bit Types**	**Fill Value**	**Valid Range**	**Scale Factor**	**Offset**
DNB_BRDF-Corrected_NTL	$nWatts \cdot cm^{-2} \cdot sr^{-1}$	BRDF corrected DNB NTL	16-bit unsigned integer	65,535	0 – 65,534	0.1	0.0
Gap_Filled_DNB_BRDF-Corrected_NTL	$nWatts \cdot cm^{-2} \cdot sr^{-1}$	Gap Filled BRDF corrected DNB NTL	16-bit unsigned integer	65,535	0 – 65,534	0.1	0.0
DNB_Lunar_Irradiance	$nWatts \cdot cm^{-2}$	DNB Lunar Irradiance	16-bit unsigned integer	65,535	0 – 65,534	0.1	0.0
Mandatory_Quality_Flag[1]	Unitless	Mandatory quality flag	8-bit unsigned integer	255	0 – 3	N/A	N/A
Latest_High_Quality_Retrieval	Number of days	Latest high quality BRDF corrected DNB radiance retrieval	8-bit unsigned integer	255	0 – 254	1.0	0.0
Snow_Flag[2]	Unitless	Flag for snow cover	8-bit unsigned integer	255	0 – 1	N/A	N/A
QF_Cloud_Mask[3]	Unitless	Quality flag for cloud mask	16-bit unsigned integer	65,535	0 – 65,534	N/A	N/A

5.2. QA Metadata

Details of flag description key and quality flags of the product VNP46A1 and VNP46A2 are shown in following tables.

Table 9 Values of QF_Cloud_Mask in the VNP46A1 product

Bit	Flag description key	Results
0	Day / Night	0=Night 1=Day
1-3	Land / Water Background	000=Land & Desert 001=Land no Desert 010=Inland Water 011=Sea Water 101=Coastal
4-5	Cloud Mask Quality	00=Poor 01=Low 10=Medium 11=High
6-7	Cloud Detection Results & Confidence Indicator	00=Confident Clear 01=Probably Clear 10=Probably Cloudy 11=Confident Cloudy
8	Shadow Detected	1=Yes 0=No
9	Cirrus Detection (IR) (BTM15-BTM16)	1=Cloud 0=No Cloud
10	Snow/ice surface	1=snow/ice 0=no snow/ice

Table 10 Values of the Mandatory_Quality_Flag in the VNP46A2 product

Value	Retrieval Quality	Algorithm Instance
00	High-Quality	Main Algorithm (Persistent Nighttime Lights)
01	High-Quality	Main Algorithm (Ephemeral Nighttime Lights)
02	Poor-Quality	Main Algorithm (Outlier, Potential cloud contamination or other issues)
255	No Retrieval	Fill Value

5.3. Spatial Projection

NASA's Black Marble product suite (VNP46) employs the standard VIIRS Land science algorithms and software that produce the DNB standard (radiance-based) products, and their corresponding ancillary layers in gridded (Level 2G, Level 3) geographic Linear Lat/Lon (LLL) format (**Figure 14**). The gridding algorithms were modified to work with the VIIRS Day/Night Band's (DNB) unique viewing geometry, which, unlike the VIIRS moderate and imagery bands, has a ground pixel footprint at a nearly constant size (742 m). The rationale behind the VIIRS DNB gridding approach is to select the nighttime observations from available 6-minute swath granules (2366 km along track, ~3100 km across-track), that are the least affected by cloud cover and off-nadir viewing observations. The goal is to increase signal-to-noise, while maximizing coverage within a cell of the gridded projection (Tan et al., 2006; Wolfe et al., 2002). By implementing this combined gridding strategy and LLL projection formats, we seek to improve the efficiency of processing and reprocessing of the VNP46 product suite, preserve the satellite location and observation footprints, while also enabling the ingest of the products into accessible software for GIS-friendly analysis and mapping.

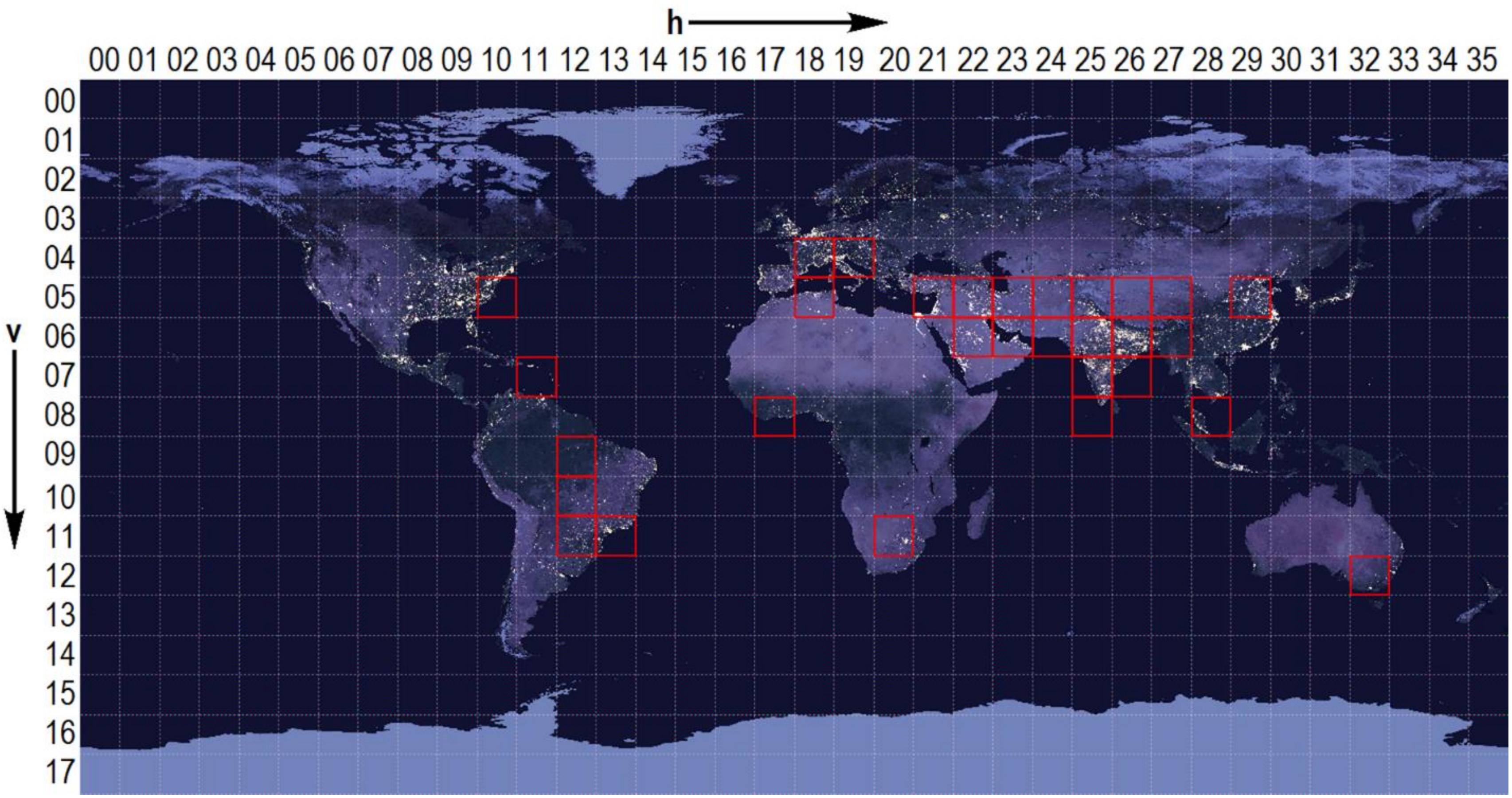

Figure 14 The Suomi-NPP VIIRS linear latitude/longitude (or geographic) grid consists of 460 non-overlapping Land tiles which measure approximately 10° x 10° region. 30 VIIRS tiles (highlighted in red) were used to conduct the benchmark tests presented in Section 4.

6. PRODUCT PUBLICATIONS

Román, M.O., Wang, Z., Sun, Q., Kalb, V., Miller, S.D., Molthan, A., Schultz, L., Bell, J., Stokes, E.C., Pandey, B. and Seto, K.C., 2018. NASA's Black Marble nighttime lights product suite. *Remote Sensing of Environment*, *210*, pp.113-143.

Cole, T.A., Wanik, D.W., Molthan, A.L., Román, M.O. and Griffin, R.E., 2017. Synergistic use of nighttime satellite data, electric utility infrastructure, and ambient population to improve power outage detections in urban areas. *Remote Sensing*, *9*(3), p.286.

Román, M.O. and Stokes, E.C., 2015. Holidays in lights: Tracking cultural patterns in demand for energy services. *Earth's Future*, *3*(6), pp.182-205.

7. REFERENCES

Andersson, E., Barthel, S., Borgström, S., Colding, J., Elmqvist, T., Folke, C., Gren, Å., 2014. Reconnecting cities to the biosphere: stewardship of green infrastructure and urban ecosystem services. Ambio 43, 445–453.

Asanuma, I., Yamaguchi, T., Park, J., Mackin, K.J., Mittleman, J., 2016. Detection limit of fishing boats by the day night band (DNB) on VIIRS, in: SPIE Optical Engineering+ Applications. International Society for Optics and Photonics, p. 99760P–99760P–8.

Bankert, R.L., Solbrig, J.E., Lee, T.F., Miller, S.D., 2011. Automated lightning flash detection in nighttime visible satellite data. Weather Forecast. 26, 399–408.

Baret, F., NightingaleJ., Garrigues, S., Justice, C., Nickeson, J.E., 2009. Report on the CEOS Land Product Validation Sub-group Meeting. Earth Obs. 21, 26–30.

Bennett, M.M., Smith, L.C., 2017. Advances in using multitemporal night-time lights satellite imagery to detect, estimate, and monitor socioeconomic dynamics. Remote Sens. Environ. 192, 176–197. doi:10.1016/j.rse.2017.01.005

Bennie, J., Davies, T.W., Inger, R., Gaston, K.J., 2014. Mapping artificial lightscapes for ecological studies. Methods Ecol. Evol. 5, 534–540. doi:10.1111/2041-210X.12182

Bickenbach, F., Bode, E., Nunnenkamp, P., Söder, M., 2016. Night lights and regional GDP. Rev. World Econ. 152, 425–447. doi:10.1007/s10290-016-0246-0

Campagnolo, M.L., Sun, Q., Liu, Y., Schaaf, C., Wang, Z., Román, M.O., 2016. Estimating the effective spatial resolution of the operational BRDF, albedo, and nadir reflectance products from MODIS and VIIRS. Remote Sens. Environ. 175, 52–64.

Cao, C., Bai, Y., 2014. Quantitative Analysis of VIIRS DNB Nightlight Point Source for Light Power Estimation and Stability Monitoring. Remote Sens. 6, 11915–11935. doi:10.3390/rs61211915

Cao, C., Shao, X., Uprety, S., 2013. Detecting light outages after severe storms using the S-NPP/VIIRS day/night band radiances. IEEE Geosci. Remote Sens. Lett. 10, 1582–1586. doi:10.1109/LGRS.2013.2262258

Cescatti, A., Marcolla, B., Vannan, S.K.S., Pan, J.Y., Román, M.O., Yang, X., Ciais, P., Cook, R.B., Law, B.E., Matteucci, G., Migliavacca, M., Moors, E., Richardson, A.D., Seufert, G.G., Schaaf, C.B., 2012. Intercomparison of MODIS albedo retrievals and in situ measurements across the global FLUXNET network. Remote Sens. Environ. 121, 323–334. doi:10.1016/j.rse.2012.02.019

Chen, H., Xiong, X., Sun, C., Chen, X., Chiang, K., 2017. Suomi-NPP VIIRS day–night band on-orbit calibration and performance. J. Appl. Remote Sens. 11, 36019.

Chen, J.M., Black, T.A., 1991. Measuring leaf area index of plant canopies with branch architecture. Agric. For. Meteorol. 57, 1–12.

Chen, J.M., Menges, C.H., Leblanc, S.G., 2005. Global mapping of foliage clumping index using multi-angular satellite data. Remote Sens. Environ. 97, 447–457.

doi:doi:10.1016/j.rse.2005.05.003

Chen, X., Nordhaus, W., 2015. A test of the new VIIRS lights data set: Population and economic output in Africa. Remote Sens. 7, 4937–4947. doi:10.3390/rs70404937

Chen, Z., Yu, B., Hu, Y., Huang, C., Shi, K., Wu, J., 2015. Estimating house vacancy rate in metropolitan areas using NPP-VIIRS nighttime light composite data. IEEE J. Sel. Top. Appl. Earth Obs. Remote Sens. 8, 2188–2197. doi:10.1109/JSTARS.2015.2418201

Chopping, M.J., 2006. Progress in retrieving canopy structure parameters from NASA multi-angle remote sensing, in: International, I. (Ed.), Proceedings of the IEEE International Geoscience & Remote Sensing Symposium, IGARSS '06 and the 27th Canadian Remote Sensing Symposium. Denver, CO, pp. 256–259.

Cinzano, P., Falchi, F., Elvidge, C.D., Baugh, K.E., 2000. The artificial night sky brightness mapped from DMSP satellite Operational Linescan System measurements. Mon. Not. R. Astron. Soc. 318, 641–657.

Cole, T.A., Wanik, D.W., Molthan, A.L., Román, M.O., Griffin, R.E., 2017. Synergistic Use of Nighttime Satellite Data, Electric Utility Infrastructure, and Ambient Population to Improve Power Outage Detections in Urban Areas. Remote Sens. 9, 286. doi:10.3390/rs9030286

Cook, B.D., Corp, L.A., Nelson, R.F., Middleton, E.M., Morton, D.C., McCorkel, J.T., Masek, J.G., Ranson, K.J., Ly, V., Montesano, P.M., 2013. NASA goddard's LiDAR, hyperspectral and thermal (G-LiHT) airborne imager. Remote Sens. 5, 4045–4066. doi:10.3390/rs5084045

Coscieme, L., Pulselli, F.M., Bastianoni, S., Elvidge, C.D., Anderson, S., Sutton, P.C., 2014. A thermodynamic geography: Night-time satellite imagery as a proxy measure of emergy. Ambio 43, 969–979. doi:10.1007/s13280-013-0468-5

Elvidge, C.D., Keith, D.M., Tuttle, B.T., Baugh, K.E., 2010. Spectral identification of lighting type and character. Sensors 10, 3961–3988.

Elvidge, C.D., Zhizhin, M., Baugh, K., Hsu, F.-C., 2015a. Automatic boat identification system for VIIRS low light imaging data. Remote Sens. 7, 3020–3036.

Elvidge, C.D., Zhizhin, M., Baugh, K., Hsu, F.-C., Ghosh, T., 2015b. Methods for global survey of natural gas flaring from visible infrared imaging radiometer suite data. Energies 9, 14.

Esch, T., Heldens, W., Hirne, A., Keil, M., Marconcini, M., Roth, A., Zeidler, J., Dech, S., Strano, E., 2017. Breaking new ground in mapping human settlements from space-The Global Urban Footprint. arXiv Prepr. arXiv1706.04862.

Esch, T., Marconcini, M., Felbier, A., Roth, A., Heldens, W., Huber, M., Schwinger, M., Taubenbock, H., Muller, A., Dech, S., 2013. Urban footprint processor-Fully automated processing chain generating settlement masks from global data of the TanDEM-X mission. IEEE Geosci. Remote Sens. Lett. 10, 1617–1621. doi:10.1109/LGRS.2013.2272953

Falchi, F., Cinzano, P., Duriscoe, D., Kyba, C.C.M., Elvidge, C.D., Baugh, K., Portnov, B.A., Rybnikova, N.A., Furgoni, R., 2016. The new world atlas of artificial night sky brightness.

Sci. Adv. 2, e1600377.

Gao, F., Morisette, J.T., Wolfe, R.E., Ederer, G., Pedelty, J., Masuoka, E., Myneni, R., Tan, B., Nightingale, J., 2008. An algorithm to produce temporally and spatially continuous MODIS LAI time series. IEEE Geosci. Remote Sens. Lett. 5, 60–64. doi:doi:10.1109/LGRS.2007.907971

Griggs, D., Stafford-smith, M., Gaffney, O., Rockström, J., Öhman, M.C., Steffen, W., Glaser, G., Kanie, N., Noble, I., 2015. Policy : Sustainable development goals for people and planet. Nature 495, 5–9. doi:10.1038/495305a

Guo, W., Lu, D., Wu, Y., Zhang, J., 2015. Mapping impervious surface distribution with integration of SNNP VIIRS-DNB and MODIS NDVI data. Remote Sens. 7, 12459–12477. doi:10.3390/rs70912459

He, L., Chen, J.M., Pisek, J., Schaaf, C.B., Strahler, A.H., 2012. Global clumping index map derived from the MODIS BRDF product. Remote Sens. Environ. 119, 118–130.

Helios Global, 2017. Helios Global World Trends [WWW Document]. URL http://www.heliosglobalinc.com/world-trends-watch/ (accessed 10.24.17).

Heynen, N., Perkins, H.A., Roy, P., 2006. The political ecology of uneven urban green space: the impact of political economy on race and ethnicity in producing environmental inequality in Milwaukee. Urban Aff. Rev. 42, 3–25.

Hill, M.J., Román, M.O., Schaaf, C.B., 2011. Dynamics of vegetation indices in tropical and subtropical savannas defined by ecoregions and Moderate Resolution Imaging Spectroradiometer (MODIS) land cover. Geocarto Int. 1–39. doi:doi:10.1080/10106049.2011.626529

Hillger, D., Kopp, T., Lee, T., Lindsey, D., Seaman, C., Miller, S., Solbrig, J., Kidder, S., Bachmeier, S., Jasmin, T., 2013. First-light imagery from Suomi NPP VIIRS. Bull. Am. Meteorol. Soc. 94, 1019–1029.

Holben, B.N., Eck, T.F., Slutsker, I., Tanré, D., Buis, J.P., Setzer, A., Vermote, E., Reagan, J.A., Kaufman, Y.J., Nakajima, T., Lavenu, F., Jankowiak, I., Smirnov, A., 1998. AERONET–A federated instrument network and data archive for aerosol characterization. Remote Sens. Environ. 66, 1–16. doi:doi:10.1016/S0034-4257(98)00031-5

Hu, C., Chen, S., Wang, M., Murch, B., Taylor, J., 2015. Detecting surface oil slicks using VIIRS nighttime imagery under moon glint: a case study in the Gulf of Mexico. Remote Sens. Lett. 6, 295–301.

Huang, Q., Yang, X., Gao, B., Yang, Y., Zhao, Y., 2014. Application of DMSP/OLS nighttime light images: A meta-analysis and a systematic literature review. Remote Sens. 6, 6844–6866. doi:10.3390/rs6086844

Jim, C.Y., 2004. Green-space preservation and allocation for sustainable greening of compact cities. Cities 21, 311–320.

Johnson, R.S., Zhang, J., Hyer, E.J., Miller, S.D., Reid, J.S., 2013. Preliminary investigations toward nighttime aerosol optical depth retrievals from the VIIRS day/night band. Atmos.

Meas. Tech. 6, 587–612.

Jönsson, P., Eklundh, L., 2004. TIMESAT—a program for analyzing time-series of satellite sensor data. Comput. Geosci. 30, 833–845.

Jönsson, P., Eklundh, L., 2002. Seasonality extraction by function fitting to time-series of satellite sensor data. IEEE Trans. Geosci. Remote Sens. 40, 1824–1832.

Kabisch, N., Haase, D., 2014. Green justice or just green? Provision of urban green spaces in Berlin, Germany. Landsc. Urban Plan. 122, 129–139.

Katz, Y., Levin, N., 2016. Quantifying urban light pollution - A comparison between field measurements and EROS-B imagery. Remote Sens. Environ. 177, 65–77. doi:10.1016/j.rse.2016.02.017

Klein, A.G., Stroeve, J., 2002. Development and validation of a snow albedo algorithm for the MODIS instrument. Ann. Glaciol. 34, 45–52.

Knyazikhin, Y., Glassy, J., Privette, J.L., Tian, Y., Lotsch, A., Zhang, Y., Wang, Y., Morisette, J.T., P.Votava, Myneni, R.B., Nemani, R.R., Running, S.W., 1999. MODIS Leaf Area Index (LAI) and Fraction of Photosynthetically Active Radiation Absorbed by Vegetation (FPAR) Product (MOD15) Algorithm Theoretical Basis Document, http://eospso.gsfc.nasa.gov/atbd/modistables.html.

Kopp, T.J., Thomas, W., Heidinger, A.K., Botambekov, D., Frey, R.A., Hutchison, K.D., Iisager, B.D., Brueske, K., Reed, B., 2014. The VIIRS Cloud Mask: Progress in the first year of S-NPP toward a common cloud detection scheme. J. Geophys. Res. Atmos. 119, 2441–2456.

Kyba, C.C.M., Ruhtz, T., Fischer, J., Hölker, F., 2011. Cloud coverage acts as an amplifier for ecological light pollution in urban ecosystems. PLoS One 6, e17307.

Kyba, C.C.M., Wagner, J.M., Kuechly, H.U., Walker, C.E., Elvidge, C.D., Falchi, F., Ruhtz, T., Fischer, J., Hölker, F., 2013. Citizen Science Provides Valuable Data for Monitoring Global Night Sky Luminance. Sci. Rep. 3, 1835. doi:10.1038/srep01835

Lacaze, R., Chen, J.M., Roujean, J.-L., Leblanc, S.G., 2002. Retrieval of vegetation clumping index using hot spot signatures measured by POLDER instrument. Remote Sens. Environ. 79, 84–95. doi:doi:10.1016/S0034-4257(01)00241-3

Leblanc, S.G., Chen, J.M., White, H.P., Latifovic, R., Lacaze, R., Roujean, J.-L., 2005. Canada-wide foliage clumping index mapping from multiangular POLDER measurements. Can. J. Remote Sens. 31, 364–376.

Lee, S., Chiang, K., Xiong, X., Sun, C., Anderson, S., 2014. The S-NPP VIIRS Day-Night Band on-orbit calibration/characterization and current state of SDR products. Remote Sens. 6, 12427–12446.

Lee, S., McIntire, J., Oudrari, H., Schwarting, T., Xiong, X., 2015. A New Method for Suomi-NPP VIIRS Day–Night Band On-Orbit Radiometric Calibration. IEEE Trans. Geosci. Remote Sens. 53, 324–334. doi:10.1109/TGRS.2014.2321835

Levin, N., 2017. The impact of seasonal changes on observed nighttime brightness from 2014 to

2015 monthly VIIRS DNB composites. Remote Sens. Environ. 193, 150–164. doi:10.1016/j.rse.2017.03.003

Levin, N., Zhang, Q., 2017. A global analysis of factors controlling VIIRS nighttime light levels from densely populated areas. Remote Sens. Environ. 190, 366–382. doi:10.1016/j.rse.2017.01.006

Li, X., Xu, H., Chen, X., Li, C., 2013. Potential of NPP-VIIRS nighttime light imagery for modeling the regional economy of China. Remote Sens. 5, 3057–3081. doi:10.3390/rs5063057

Liao, L.B., Weiss, S., Mills, S., Hauss, B., 2013. Suomi NPP VIIRS day-night band on-orbit performance. J. Geophys. Res. Atmos. 118, 12705–12718. doi:10.1002/2013JD020475

Liu, Y., Wang, Z., Sun, Q., Erb, A.M., Li, Z., Schaaf, C.B., Zhang, X., Román, M.O., Scott, R.L., Zhang, Q., 2017. Evaluation of the VIIRS BRDF, Albedo and NBAR products suite and an assessment of continuity with the long term MODIS record. Remote Sens. Environ. 201, 256–274.

Liu, Hu, C., Zhan, W., Sun, C., Murch, B., Ma., L., 2017. Identifying industrial heat sources using time-series of the VIIRS Nightfire product with an object-oriented approach. Remote Sens. Environ. doi:10.1016/J.RSE.2017.10.019

Lucht, W., Roujean, J., 2000. Considerations in the parametric modeling of BRDF and albedo from multiangular satellite sensor observations. Remote Sens. Rev. 18, 343–379.

Ma, T., Zhou, C.H., Pei, T., Haynie, S., Fan, J.F., 2014. Responses of Suomi- NPP VIIRS-derived nighttime lights to socioeconomic activity in China’s cities. Remote Sens. Lett. 5, 165–174. doi:10.1080/2150704x.2014.890758

Mann, M.L., Melaas, E.K., Malik, A., 2016. Using VIIRS Day/Night Band to Measure Electricity Supply Reliability: Preliminary Results from Maharashtra, India. Remote Sens. 8, 711.

McHardy, T.M., Zhang, J., Reid, J.S., Miller, S.D., Hyer, E.J., Kuehn, R.E., 2015. An improved method for retrieving nighttime aerosol optical thickness from the VIIRS Day/Night Band. Atmos. Meas. Tech. 8, 4773–4783.

Miller, S.D., Combs, C.L., Kidder, S.Q., Lee, T.F., 2012. Assessing Moonlight Availability for Nighttime Environmental Applications by Low-Light Visible Polar-Orbiting Satellite Sensors. J. Atmos. Ocean. Technol. 29, 538–557. doi:10.1175/JTECH-D-11-00192.1

Miller, S.D., Haddock, S.H.D., Elvidge, C.D., Lee, T.F., 2006. Twenty thousand leagues over the seas: the first satellite perspective on bioluminescent “milky seas.” Int. J. Remote Sens. 27, 5131–5143. doi:10.1080/01431160600554298

Miller, S.D., Haddock, S.H.D., Elvidge, C.D., Lee, T.F., 2005. Detection of a bioluminescent milky sea from space. PNAS 102, 14181–14184. doi:doi:10.1073/pnas.0507253102

Miller, S.D., Straka, W., Mills, S.P., Elvidge, C.D., Lee, T.F., Solbrig, J., Walther, A., Heidinger, A.K., Weiss, S.C., 2013. Illuminating the capabilities of the suomi national polar-orbiting partnership (NPP) visible infrared imaging radiometer suite (VIIRS) day/night band.

Remote Sens. 5, 6717–6766.

Miller, S.D., Straka, W.C., Yue, J., Smith, S.M., Alexander, M.J., Hoffmann, L., Setvák, M., Partain, P.T., 2015. Upper atmospheric gravity wave details revealed in nightglow satellite imagery. Proc. Natl. Acad. Sci. 112, E6728–E6735.

Miller, S.D., Turner, R.E., 2009. A Dynamic Lunar Spectral Irradiance Data Set for NPOESS/VIIRS Day/Night Band Nighttime Environmental Applications. IEEE Trans. Geosci. Remote Sens. 47, 2316–2329. doi:10.1109/TGRS.2009.2012696

Miller, Mills, S.P., Elvidge, C.D., Lindsey, D.T., Lee, T.F., Hawkins, J.D., 2012. Suomi satellite brings to light a unique frontier of nighttime environmental sensing capabilities. Proc. Natl. Acad. Sci. 109, 15706–15711. doi:doi:10.1073/pnas.1207034109

Mills, S., Miller, S., 2016. VIIRS Day/Night Band—Correcting Striping and Nonuniformity over a Very Large Dynamic Range. J. Imaging 2, 9. doi:doi:10.3390/jimaging2010009

Mills, S., Weiss, S., Liang, C., 2013. VIIRS day/night band (DNB) stray light characterization and correction, in: SPIE Optical Engineering+ Applications. International Society for Optics and Photonics, p. 88661P–88661P.

Minnis, P., Hong, G., Sun-Mack, S., Smith, W.L., Chen, Y., Miller, S.D., 2016. Estimating nocturnal opaque ice cloud optical depth from MODIS multispectral infrared radiances using a neural network method. J. Geophys. Res. Atmos. 121, 4907–4932. doi:10.1002/2015JD024456

Molthan, A., Jedlovec, G., 2013. Satellite observations monitor outages from Superstorm Sandy. Eos, Trans. Am. Geophys. Union 94, 53–54.

Moody, E.G., King, M.D., Schaaf, C.B., Platnick, S., 2008. MODIS-derived spatially complete surface albedo products: Spatial and temporal pixel distribution and zonal averages. J. Appl. Meteorol. Climatol. 47, 2879–2894. doi:doi:10.1175/2008JAMC1795.1

Moorthi, S., Pan, H.-L., Caplan, P., 2001. Changes to the 2001 NCEP operational MRF/AVN global analysis/forecast system. US Department of Commerce, National Oceanic and Atmospheric Administration, National Weather Service, Office of Meteorology, Program and Plans Division.

Morisette, J.T., Baret, F., Liang, S., 2006. Special issue on global land product validation. IEEE Trans. Geosci. Remote Sens. 44, 1695–1697.

Moustafa, S.E., Rennermalm, A.K., Román, M.O., Wang, Z., Schaaf, C.B., Smith, L.C., Koenig, L.S., Erb, A., 2017. Evaluation of satellite remote sensing albedo retrievals over the ablation area of the southwestern Greenland ice sheet. Remote Sens. Environ. 198, 115–125.

NASM, 2018. Thriving on Our Changing Planet: A Decadal Strategy for Earth Observation from Space. The National Academies Press, Washington, DC. doi:10.17226/24938

Nicodemus, F.E., 1977. Geometrical considerations and nomenclature for reflectance, in: National Bureau of Standards Monograph, No. 160. Washington, DC, pp. 1–52.

Nilson, T., 1971. A theoretical analysis of the frequency of gaps in plant stands. Agric. Meteorol. 8, 25–38.

NRC, 2017. A look into Zaatari camp during winter | NRC [WWW Document]. World Bank. URL https://www.nrc.no/news/2016/february/a-look-into-zaatari-camp-during-winter/ (accessed 10.24.17).

O'Sullivan, F., 2017. How Built-Out Barcelona Found Space for an Urban Forest - CityLab [WWW Document]. URL https://www.citylab.com/solutions/2017/05/barcelona-green-urban-forest-climate-plan/526998/ (accessed 6.28.17).

Oda, T., Lauvaux, T., Lu, D., Rao, P., Miles, N.L., Richardson, S.J., Gurney, K.R., 2017. On the impact of granularity of space-based urban CO 2 emissions in urban atmospheric inversions: A case study for Indianapolis, IN. Elem Sci Anth 5.

Omar, A.H., Winker, D.M., Tackett, J.L., Giles, D.M., Kar, J., Liu, Z., Vaughan, M.A., Powell, K.A., Trepte, C.R., 2013. CALIOP and AERONET aerosol optical depth comparisons: One size fits none. J. Geophys. Res. Atmos. 118, 4748–4766.

Ou, J., Liu, X., Li, X., Li, M., Li, W., 2015. Evaluation of NPP-VIIRS nighttime light data for mapping global fossil fuel combustion CO 2 emissions: a comparison with DMSP-OLS nighttime light data. PLoS One 10, e0138310. doi:10.1371/journal.pone.0138310

Pahlevan, N., Sarkar, S., Devadiga, S., Wolfe, R.E., Román, M., Vermote, E., Lin, G., Xiong, X., 2017. Impact of Spatial Sampling on Continuity of MODIS–VIIRS Land Surface Reflectance Products: A Simulation Approach. IEEE Trans. Geosci. Remote Sens. 55, 183–196.

Park, T., Yan, K., Chen, C., Xu, B., Knyazikhin, Y., Myneni, R., 2017. VIIRS Leaf Area Index (LAI) and Fraction of Photosynthetically Active Radiation Absorbed by Vegetation (FPAR) Product Algorithm Theoretical Basis Document (ATBD), NASA Technical Report.

Paynter, I., Saenz, E., Genest, D., Peri, F., Erb, A., Li, Z., Wiggin, K., Muir, J., Raumonen, P., Schaaf, E.S., 2016. Observing ecosystems with lightweight, rapid-scanning terrestrial lidar scanners. Remote Sens. Ecol. Conserv. 2, 174–189.

Polivka, T.N., Wang, J., Ellison, L.T., Hyer, E.J., Ichoku, C.M., 2016. Improving Nocturnal Fire Detection With the VIIRS Day–Night Band. IEEE Trans. Geosci. Remote Sens. 54, 5503–5519.

Riggs, G.A., Hall, D.K., Román, M.O., 2017. Overview of NASA's MODIS and VIIRS Snow-Cover Earth System Data Records. Earth Syst. Sci. Data 9, 1–13. doi:10.5194/essd-9-765-2017

Riggs, G.A., Hall, D.K., Román, M.O., 2016. NASA S-NPP VIIRS Snow Products Collection 1 User Guide 1–26. doi:doi:10.5067/VIIRS/VNP10_L2.v001

Roger, J.C., Vermote, E.F., Devadiga, S., Ray, J.P., 2016. Suomi-NPP VIIRS Surface Reflectance User's Guide.

Román, M., Schaaf, C.B., Yang, X., Woodcock, C.E., Strahler, A.H., Braswell, R.H., Curtis, P.S., Davis, K.J., D., D., Gu, L., Goulden, M.L., Hollinger, D.Y., Kolb, T.E., Meyers, T.P., Munger, J.W., Privette, J.L., Richardson, A.D., Wilson, T.B., Wofsy, S.C., 2009. The MODIS (Collection V005) BRDF/albedo product: Assessment of spatial representativeness over forested landscapes. Remote Sens. Environ. 113, 2476–2498. doi:doi:10.1016/j.rse.2009.07.009

Román, M.O., Gatebe, C.K., Poudyal, R., Schaaf, C.B., Wang, Z., King, M.D., 2011. Variability in surface BRDF at different spatial scales (30 m-500 m) over a mixed agricultural landscape as retrieved from airborne and satellite spectral measurements. Remote Sens. Environ. 115, 2184–2203. doi:10.1016/j.rse.2011.04.012

Román, M.O., Gatebe, C.K., Shuai, Y., Wang, Z., Gao, F., Masek, J.G., He, T., Liang, S., Schaaf, C.B., 2013. Use of In Situ and Airborne Multiangle Data to Assess MODIS- and Landsat-Based Estimates of Directional Reflectance and Albedo. IEEE Trans. Geosci. Remote Sens. 51, 1393–1404. doi:10.1109/TGRS.2013.2243457

Román, M.O., Schaaf, C.B., Lewis, P., Gao, F., Anderson, G.P., Privette, J.L., Strahler, A.H., Woodcock, C.E., Barnsley, M., 2010. Assessing the coupling between surface albedo derived from MODIS and the fraction of diffuse skylight over spatially-characterized landscapes. Remote Sens. Environ. 114, 738–760. doi:10.1016/j.rse.2009.11.014

Román, M.O., Stokes, E.C., 2015. Holidays in lights: Tracking cultural patterns in demand for energy services. Earth's Futur. 3, 182–205. doi:10.1002/2014EF000285

Roujean, J., Leroy, M., Deschanms, P., 1992. A bidirectional reflectance model of the Earth's surface for the correction of remote sensing data. J. Geophys. Res. 97, 20,420-455,468. doi:doi:10.1029/92JD01411

Schaaf, C.B., Gao, F., Strahler, A.H., Lucht, W., Li, X., Tsang, T., Strugnell, N.C., Zhang, X., Jin, Y., Muller, J.P.J.-P., Lewis, P., Barnsley, M., Hobson, P., Disney, M., Roberts, G., Dunderdale, M., Doll, C., d'Entremont, R.P., Hu, B., Liang, S., Privette, J.L., Roy, D.P., 2002. First operational BRDF, albedo nadir reflectance products from MODIS. Remote Sens. Environ. 83, 135–148. doi:10.1016/S0034-4257(02)00091-3

Schaaf, Liu, J., Gao, F., Strahler, A.H., 2011a. MODIS albedo and reflectance anisotropy products from Aqua and Terra, in: Ramachandran, B., Justice, C., Abrams, M. (Eds.), Land Remote Sensing and Global Environmental Change: NASA's Earth Observing System and the Science of ASTER and MODIS. Springer-Verlag. ISBN:1441967486., p. 873.

Schaaf, Wang, Z., Strahler, A., 2011b. Commentary on Wang and Zender—MODIS snow albedo bias at high solar zenith angles relative to theory and to in situ observations in Greenland. Remote Sens. Environ. 115, 1296–1300.

Schaepman-Strub, G., Schaepman, M.E., Painter, T.H., Dangel, S., Martonchik, J. V, 2006. Reflectance quantities in optical remote sensing-definitions and case studies. Remote Sens. Environ. 103, 27–42. doi:doi:10.1016/j.rse.2006.03.002

Schnitt, S., Ruhtz, T., Fischer, J., Hölker, F., Kyba, C., 2013. Temperature stability of the sky quality meter. Sensors 13, 12166–12174.

Seto, K.C., Dhakal, S., 2014. Chapter 12: Human Settlements, Infrastructure, and Spatial

Planning. Clim. Chang. 2014 Mitig. Clim. Chang. Contrib. Work. Gr. III to Fifth Assess. Rep. Intergov. Panel Clim. Chang. 67–76.

Sharma, R.C., Tateishi, R., Hara, K., Gharechelou, S., Iizuka, K., 2016. Global mapping of urban built-up areas of year 2014 by combining MODIS multispectral data with VIIRS nighttime light data. Int. J. Digit. Earth 9, 1004–1020. doi:10.1080/17538947.2016.1168879

Shi, K., Huang, C., Yu, B., Yin, B., Huang, Y., Wu, J., Chang, H., Bailang, Y., Bing, Y., Yixiu, H., Jianping, W., 2014. Evaluation of NPP-VIIRS night-time light composite data for extracting built-up urban areas. Remote Sens. Lett. 5, 358–366. doi:10.1080/2150704x.2014.905728

Shuai, Y., Schaaf, C., Zhang, X., Strahler, A., Roy, D., Morisette, J., Wang, Z., Nightingale, J., Nickeson, J., Richardson, A.D., 2013. Daily MODIS 500 m reflectance anisotropy direct broadcast (DB) products for monitoring vegetation phenology dynamics. Int. J. Remote Sens. 34, 5997–6016.

Skakun, S., Justice, C.O., Vermote, E., Roger, J.-C., 2018. Transitioning from MODIS to VIIRS: an analysis of inter-consistency of NDVI data sets for agricultural monitoring. Int. J. Remote Sens. 39, 971–992.

Strahler, A.H., Lucht, W., Schaaf, C.B., Tsang, T., Gao, F., Li, X., Muller, J.-P., Lewis, P., Barnsley, M., 1999. MODIS BRDF/Albedo Product: Algorithm Theoretical Basis Document Version 5.0. Technical Report. NASA EOS-MODIS.

Straka, W.C., Seaman, C.J., Baugh, K., Cole, K., Stevens, E., Miller, S.D., 2015. Utilization of the suomi national polar-orbiting partnership (npp) visible infrared imaging radiometer suite (viirs) day/night band for arctic ship tracking and fisheries management. Remote Sens. 7, 971–989.

Strugnell, N., Lucht, W., Schaaf, C.B., 2001. A global albedo data set derived from AVHRR data for use in climate simulations. Geophys. Res. Lett. 28, 191–194. doi:doi:10.1029/2000GL011580

Sun, Q., Wang, Z., Li, Z., Erb, A., Schaaf, C.B., 2017. Evaluation of the global MODIS 30 arc-second spatially and temporally complete snow-free land surface albedo and reflectance anisotropy dataset. Int. J. Appl. Earth Obs. Geoinf. 58, 36–49.

Tan, B., Morisette, J.T., Wolfe, R.E., Gao, F., Ederer, G.A., Nightingale, J., Pedelty, J.A., 2011. An Enhanced TIMESAT Algorithm for Estimating Vegetation Phenology Metrics From MODIS Data. Ieee J. Sel. Top. Appl. Earth Obs. Remote Sens. 4, 361–371. doi:Doi 10.1109/Jstars.2010.2075916

Tan, B., Morisette, J.T., Wolfe, R.E., Gao, F., Ederer, G.A., Nightingale, J., Pedelty, J.A., 2008. Vegetation phenology metrics derived from temporally smoothed and gap-filled MODIS data, in: Geoscience and Remote Sensing Symposium, 2008. IGARSS 2008. IEEE International. IEEE, p. III-593.

Tan, B., Woodcock, C.E., Hu, J., Zhang, P., Ozdogan, M., Huang, D., Yang, W., Knyazikhin, Y., Myneni, R.B., 2006. The impact of gridding artifacts on the local spatial properties of MODIS data: Implications for validation, compositing, and band-to-band registration across resolutions. Remote Sens. Environ. 105, 98–114.

Thaiutsa, B., Puangchit, L., Kjelgren, R., Arunpraparut, W., 2008. Urban green space, street tree and heritage large tree assessment in Bangkok, Thailand. Urban For. urban Green. 7, 219–229.

Tomasi, C., Fuzzi, S., Kokhanovsky, A., 2017. Atmospheric Aerosols: Life Cycles and Effects on Air Quality and Climate. John Wiley & Sons.

UNHCR, 2017. Syria Regional Refugee Response - - - Emirati Jordanian Camp (Murijep al Fhoud) [WWW Document]. URL http://data.unhcr.org/syrianrefugees/settlement.php?id=224&country=0&region=0 (accessed 10.25.17).

Vermote, E., Justice, C.O., Csiszar, I., 2014. Early evaluation of the VIIRS calibration, cloud mask and surface reflectance Earth data records. Remote Sens. Environ. 148, 134–145. doi:10.1016/j.rse.2014.03.028

Vermote, E.F., Kotchenova, S., 2008. Atmospheric correction for the monitoring of land surfaces. J. Geophys. Res. 113. doi:doi:10.1029/2007JD009662.

Walther, A., Heidinger, A.K., Miller, S., 2013. The Expected Performance of Cloud Optical and Microphysical Properties derived from Soumi NPP VIIRS Day/Night Band Lunar Reflectance. J. Geophys. Res. Atmos. 2013JD020478. doi:10.1002/2013JD020478

Wang, J., Aegerter, C., Xu, X., Szykman, J.J., 2016. Potential application of VIIRS Day/Night Band for monitoring nighttime surface PM 2.5 air quality from space. Atmos. Environ. 124, 55–63.

Wang, Z., Schaaf, C.B., Strahler, A.H., Chopping, M.J., Román, M.O., Shuai, Y., Woodcock, C.E., Hollinger, D.Y., Fitzjarrald, D.R., 2014. Evaluation of MODIS albedo product (MCD43A) over grassland, agriculture and forest surface types during dormant and snow-covered periods. Remote Sens. Environ. 140, 60–77. doi:10.1016/j.rse.2013.08.025

Wang, Z., Schaaf, C.B., Strahler, A.H., Wang, J., Woodcock, C.E., Chopping, M.J., Román, M.O., Rocha, A. V, Shuai, Y., 2012. Evaluation of Moderate-resolution Imaging Spectroradiometer (MODIS) snow albedo product (MCD43A) over tundra. Remote Sens. Environ. 117, 264–280. doi:doi:10.1016/j.rse.2011.10.002

Wickland, D., Gobron, N., Moore, B., Nakajima, M., Sathyendranath, S., Plummer, S., Schmullius, C., Dubayah, R., 2014. CEOS Strategy for Carbon Observations from Space. 40th COSPAR Sci. Assem. Held 2-10 August 2014, Moscow, Russ. Abstr. A0. 1-2-14. 40, 3626.

WMO, 2016. Observing Systems Capabilities Analysis and Review tool: Rolling Requirements Review process [WWW Document]. URL http://www.wmo.int/pages/prog/www/OSY/RRR-DB.html (accessed 8.25.17).

Wolch, J.R., Byrne, J., Newell, J.P., 2014. Urban green space, public health, and environmental justice: The challenge of making cities "just green enough." Landsc. Urban Plan. 125, 234–244.

Wolfe, R.E., Lin, G., Nishihama, M., Tewari, K.P., Tilton, J.C., Isaacman, A.R., 2013. Suomi NPP VIIRS prelaunch and on-orbit geometric calibration and characterization. J. Geophys. Res. Atmos. 118.

Wolfe, R.E., Nishihama, M., Fleig, A.J., Kuyper, J.A., Roy, D.P., Storey, J.C., Patt, F.S., 2002. Achieving sub-pixel geolocation accuracy in support of MODIS land science. Remote Sens. Environ. 83, 31–49.

Wolfe, R.E., Roy, D.P., Vermote, E., 1998. MODIS land data storage, gridding, and compositing methodology: Level 2 grid. IEEE Trans. Geosci. Remote Sens. 36, 1324–1338.

World Bank, 2017. Rebuilding Infrastructure and Improving Access to Employment in Post Crisis Côte d'Ivoire [WWW Document]. World Bank. URL http://www.worldbank.org/en/results/2016/06/17/rebuilding-infrastructure-and-improving-access-to-employment-in-post-crisis-cote-divoire (accessed 10.24.17).

Xiao, Z., Liang, S., Wang, T., Jiang, B., 2016. Retrieval of Leaf Area Index (LAI) and Fraction of Absorbed Photosynthetically Active Radiation (FAPAR) from VIIRS Time-Series Data. Remote Sens. 8, 351.

Xiong, X., Butler, J., Chiang, K., Efremova, B., Fulbright, J., Lei, N., McIntire, J., Oudrari, H., Sun, J., Wang, Z., 2014. VIIRS on-orbit calibration methodology and performance. J. Geophys. Res. Atmos. 119, 5065–5078.

Yang, K., Wolfe, R.E., 2001. MODIS level 2 grid with the ISIN map projection, in: Geoscience and Remote Sensing Symposium, 2001. IGARSS'01. IEEE 2001 International. IEEE, pp. 3291–3293.

Yorks, J., Palm, S., McGill, M., Hlavka, D., Hart, W., Selmer, P., Nowottnick, E., 2015. CATS Algorithm Theoretical Basis Document Level 1 and Level 2 Data Products Release 1.

Yorks, J.E., McGill, M.J., Palm, S.P., Hlavka, D.L., Selmer, P.A., Nowottnick, E.P., Vaughan, M.A., Rodier, S.D., Hart, W.D., 2016. An overview of the CATS level 1 processing algorithms and data products. Geophys. Res. Lett. 43, 4632–4639. doi:10.1002/2016GL068006

Yu, B., Shi, K., Hu, Y., Huang, C., Chen, Z., Wu, J., 2015. Poverty evaluation using NPP-VIIRS nighttime light composite data at the county level in China. IEEE J. Sel. Top. Appl. Earth Obs. Remote Sens. 8, 1217–1229. doi:10.1109/JSTARS.2015.2399416

Zhang, Q., Pandey, B., Seto, K.C., 2016. A Robust Method to Generate a Consistent Time Series From DMSP/OLS Nighttime Light Data. IEEE Trans. Geosci. Remote Sens. 54, 5821–5831.

Zhao, F., Strahler, A.H., Schaaf, C., Yao, T., Yang, X., Wang, Z., Schull, M.A., Román, M.O., Woodcock, C.E., Olofsson, P., Ni-Meister, W., Jupp, D.L.B., Lovell, J.L., Culvenor, D.S., Newnham, G.J., 2012. Measuring Gap Fraction, Element Clumping Index and LAI in Sierra Forest Stands Using a Full-waveform Ground-Based Lidar. Remote Sens. Environ. 125, 73–79. doi:doi:10.1016/j.rse.2012.07.007

Zhao, X., Shi, H., Yu, H., Yang, P., 2016. Inversion of Nighttime PM2. 5 Mass Concentration in Beijing Based on the VIIRS Day-Night Band. Atmosphere (Basel). 7, 136.